

MODELING THERMAL DUST EMISSION WITH TWO COMPONENTS: APPLICATION TO THE *PLANCK* HIGH FREQUENCY INSTRUMENT MAPS

AARON M. MEISNER^{1,2} AND DOUGLAS P. FINKBEINER^{1,2}

¹ Department of Physics, Harvard University, 17 Oxford Street, Cambridge, MA 02138, USA; ameisner@fas.harvard.edu

² Harvard-Smithsonian Center for Astrophysics, 60 Garden Street, Cambridge, MA 02138, USA; dfinkbeiner@cfa.harvard.edu

Received 2014 August 11; accepted 2014 October 27; published 2014 December 30

ABSTRACT

We apply the Finkbeiner et al. two-component thermal dust emission model to the *Planck* High Frequency Instrument maps. This parameterization of the far-infrared dust spectrum as the sum of two modified blackbodies (MBBs) serves as an important alternative to the commonly adopted single-MBB dust emission model. Analyzing the joint *Planck*/DIRBE dust spectrum, we show that two-component models provide a better fit to the 100–3000 GHz emission than do single-MBB models, though by a lesser margin than found by Finkbeiner et al. based on FIRAS and DIRBE. We also derive full-sky 6.1' resolution maps of dust optical depth and temperature by fitting the two-component model to *Planck* 217–857 GHz along with DIRBE/*IRAS* 100 μm data. Because our two-component model matches the dust spectrum near its peak, accounts for the spectrum's flattening at millimeter wavelengths, and specifies dust temperature at 6.1' FWHM, our model provides reliable, high-resolution thermal dust emission foreground predictions from 100 to 3000 GHz. We find that, in diffuse sky regions, our two-component 100–217 GHz predictions are on average accurate to within 2.2%, while extrapolating the Planck Collaboration et al. single-MBB model systematically underpredicts emission by 18.8% at 100 GHz, 12.6% at 143 GHz, and 7.9% at 217 GHz. We calibrate our two-component optical depth to reddening, and compare with reddening estimates based on stellar spectra. We find the dominant systematic problems in our temperature/reddening maps to be zodiacal light on large angular scales and the cosmic infrared background anisotropy on small angular scales.

Key words: dust, extinction – infrared: ISM – submillimeter: ISM

1. INTRODUCTION

The presence of Galactic interstellar dust affects astronomical observations over a wide range of wavelengths. In the mid-infrared (IR) and far-infrared (FIR), Galactic dust emission contributes significantly to the total observed sky intensity. At optical and ultraviolet (UV) wavelengths, dust grains absorb and scatter starlight. Observations of interstellar dust emission/absorption can improve our understanding of the physical conditions and composition of the interstellar medium (ISM), an environment that plays a crucial role in Galactic evolution and star formation. Equally, or perhaps even more important to the practice of astronomy, however, is accurately accounting for dust as a foreground that reddens optical/UV observations of stars/galaxies and superimposes Galactic emission on low-frequency observations of the cosmic microwave background (CMB).

Over the past decades, satellite observations have dramatically enhanced our knowledge about IR emission from the ISM. The *Infrared Astronomy Satellite* (*IRAS*), with its $\sim 4'$ resolution, revolutionized the study of Galactic dust emission, first revealing the high-latitude “IR cirrus” using 60 μm and 100 μm observations (Low et al. 1984; Wheelock et al. 1994) and highlighting the importance of detailed dust mapping in the FIR/submillimeter as a key foreground for cosmology. Later, the Diffuse IR Background Experiment (DIRBE) aboard the *COBE* satellite provided complementary full-sky measurements at 10 IR wavelengths from 1.25 μm to 240 μm , boasting a reliable zero point despite inferior $\sim 0.7'$ angular resolution (Boggess et al. 1992). *COBE*/*FIRAS* (Mather 1982) also provided full-sky IR dust spectra at 7° resolution in 213 narrow frequency bins between 30 GHz and 2850 GHz.

Finkbeiner et al. (1999, hereafter FDS99) used these FIRAS data to derive a globally best-fit model of dust emission applicable over a very broad range of frequencies. FDS99 showed that no model consisting of a single modified blackbody (MBB) could accurately match the FIRAS/DIRBE spectrum at both the Wien and Rayleigh–Jeans extremes. To fit the thermal dust spectrum between 100 and 3000 GHz, FDS99 therefore proposed an emission model consisting of two MBBs, each with a different temperature and emissivity power-law index. Physically, these two components might represent distinct dust grain species within the ISM, or they might simply provide a convenient fitting function. By combining this best-fit two-component model with a custom reprocessing of DIRBE and *IRAS* 100 μm data, FDS99 provided widely used foreground predictions with 6.1' FWHM, limited largely by their 1.3' resolution DIRBE-based temperature correction.

The *Planck* 2013 data release (Planck Collaboration et al. 2013b) represents an important opportunity to revisit foreground predictions in light of *Planck*'s superb, relatively artifact-free broadband data covering the entire sky and a wide range of frequencies. Toward this end, Planck Collaboration et al. (2013a) have conducted a study modeling *Planck* 353 GHz, 545 GHz, 857 GHz, and DIRBE/*IRAS* 100 μm emission with a single-MBB spectrum. More recently, Planck Collaboration et al. (2014) have applied the Draine & Li (2007) dust grain model to *Planck*, *IRAS*, and *WISE* emission between 353 GHz and 12 μm . Here we investigate the FDS99 two-component dust emission model as an alternative parameterization for the 100–3000 GHz dust spectral energy distribution (SED) composed of *Planck* High Frequency Instrument (HFI), DIRBE, and *IRAS* data. In doing so, we obtain *Planck*-based maps of dust temperature and optical depth, both at 6.1' resolution.

Because we employ a model that has been validated with FIRAS down to millimeter wavelengths and optimized for *Planck*, our derived parameters are useful in constructing high-resolution predictions of dust emission over a very broad range of wavelengths. This includes low frequencies (100–350 GHz), which Planck Collaboration et al. (2013a) caution their model may not adequately fit, and also wavelengths near the peak of the dust SED, relevant to, e.g., *Akari* 140–160 μm (Doi et al. 2012). We also anticipate that our derived optical depth map will serve as a valuable cross-check for extinction estimates based directly upon optical observations of stars (e.g., Schlafly et al. 2014) and as a baseline for next-generation dust extinction maps incorporating high-resolution, full-sky IR data sets such as *WISE* (Wright et al. 2010; Meisner & Finkbeiner 2014) and *Akari*.

In Section 2, we introduce the data used throughout this study. In Section 3, we describe our preprocessing of the *Planck* maps to isolate thermal emission from Galactic dust. In Section 4, we explain the two-component emission model we apply to the *Planck*-based dust SED. In Section 5, we discuss the details of predicting *Planck* observations based on this dust model. In Section 6, we derive constraints on our model’s global parameters in light of the *Planck* HFI maps. In Section 7, we detail the Markov chain Monte Carlo (MCMC) method with which we have estimated the spatially varying parameters of our model. In Section 8, we calibrate our derived optical depth to reddening at optical wavelengths. In Section 9, we compare our two-component thermal dust emission predictions to those of Planck Collaboration et al. (2013a). In Section 10, we present the full-sky maps of dust temperature and optical depth we have obtained, and conclude in Section 11.

2. DATA

All *Planck* data products utilized throughout this work are drawn from the *Planck* 2013 release (Planck Collaboration et al. 2013b). Specifically, we have made use of all six of the zodiacal light corrected HFI intensity maps (R1.10_nominal_ZodiCorrected; Planck Collaboration et al. 2013h). Our full-resolution (6.1 FWHM) SED fits neglect the two lowest HFI frequencies, 100 and 143 GHz, as these have FWHM of 9.66 and 7.27, respectively.

To incorporate measurements on the Wien side of the dust emission spectrum, we include 100 μm data in our SED fits. In particular, we use the Schlegel et al. (1998, henceforth SFD) reprocessing of DIRBE/IRAS 100 μm , which we will refer to as *i*100, and at times by frequency as 3000 GHz. The *i*100 map has angular resolution of 6.1, and was constructed so as to contain only thermal emission from Galactic dust, with compact sources and zodiacal light removed, and its zero level tied to H I. We use the *i*100 map as is, without any custom modifications.

In some of our FIR dust SED analyses which do not require high angular resolution, specifically those of Sections 6, 7.4, and 7.5, we also make use of the SFD reprocessings of DIRBE 140 μm (2141 GHz) and 240 μm (1250 GHz).

3. PREPROCESSING

The following subsections detail the processing steps we have applied to isolate Galactic dust emission in the *Planck* maps in preparation for SED fitting.

3.1. CMB Anisotropy Removal

We first addressed the CMB anisotropies before performing any of the interpolation/smoothing described in

Section 3.2/Section 3.3. The CMB anisotropies are effectively imperceptible upon visual inspection of *Planck* 857 GHz, but can be perceived at a low level in *Planck* 545 GHz, and are prominent at 100–353 GHz relative to the Galactic emission we wish to characterize, especially at high latitudes. To remove the CMB anisotropies, we have subtracted the Spectral Matching Independent Component Analysis (SMICA; Planck Collaboration et al. 2013f) model from each of the *Planck* maps, applying appropriate unit conversions for the 545 and 857 GHz maps with native units of MJy sr^{-1} . Low-order corrections, particularly our removal of solar dipole residuals, are discussed in Section 3.5.

3.2. Compact Sources

After subtracting the SMICA CMB model, we interpolate over compact sources, including both point sources and resolved galaxies. Removing compact sources at this stage is important as it prevents contamination of compact-source-free pixels in our downstream analyses which require smoothing of the *Planck* maps. SFD carefully removed point sources and galaxies from the *i*100 map everywhere outside of $|b| < 5^\circ$. We do not perform any further modifications of the *i*100 map to account for compact sources. To mask compact sources in the *Planck* 217–857 GHz maps, we use the SFD compact source mask. At 100, 143 GHz we use the compact source masks provided by the *Planck* collaboration in the file *HFI_Mask_PointSrc_2048_R1.10.fits*. Given our pixelization (see Section 7.1), 1.56% of pixels are masked at 217–857 GHz (1.05%, 1.02% at 100, 143 GHz).

3.3. Smoothing

For our full-resolution model, we wish to simultaneously fit *i*100 along with the four highest-frequency *Planck* bands. To properly combine these maps, they must have the same point-spread function (PSF). *i*100, with its 6.1 symmetric Gaussian beam, has the lowest angular resolution of the relevant maps. To match PSFs, we have therefore smoothed each of the *Planck* maps under consideration to *i*100 resolution by considering each native *Planck* map to have a symmetric Gaussian beam and smoothing by the appropriate symmetric Gaussian such that the resulting map has a 6.1 FWHM. The FWHM values we assign to the native *Planck* maps are taken from Planck Collaboration et al. (2013d), and are listed in Table 1.

3.4. Molecular Emission

Because the FIRAS spectra consist of many narrow frequency bins, FDS99 were able to discard the relatively small number of frequency intervals contaminated by strong molecular line emission. Unfortunately, while the *Planck* data considered in this study are of high angular resolution, the broad *Planck* bandpasses do not allow us to adopt the same approach as FDS99 in dealing with line emission. Instead, we must subtract estimates of the molecular line contamination from each *Planck* band in order to best isolate the thermal continuum we wish to characterize. The most prominent molecular line emission in the *Planck* bands of interest arises from the three lowest CO rotational transitions: $J = 1 \rightarrow 0$ at 115 GHz, $J = 2 \rightarrow 1$ at 230 GHz, and $J = 3 \rightarrow 2$ at 345 GHz, respectively, affecting the *Planck* 100, 217, and 353 GHz bands. The $J = 1 \rightarrow 0$ line also imparts a signal upon *Planck* 143 GHz, but at a negligible level, $\sim 1000 \times$ fainter relative to the dust continuum than $J = 1 \rightarrow 0$ at 100 GHz. More specifically, the ratio of $J = 1 \rightarrow 0$ intensity

Table 1
Input Map Properties and Preprocessing

ν (GHz)	Instrument(s)	Offset (K_{CMB})	Dipole (K_{CMB})	$s_{857,\nu} \times u_\nu$	$\sigma_{s_{857,\nu}} \times u_\nu$	n_ν (K_{CMB})	c_ν	FWHM (''')
100	<i>Planck</i> HFI	$1.69 \times 10^{-5} \pm 3.61 \times 10^{-7}$	-1.08×10^{-5}	1.46×10^{-3}	2.92×10^{-5}	7.77×10^{-5}	0.0054	9.66
143	<i>Planck</i> HFI	$3.58 \times 10^{-5} \pm 7.58 \times 10^{-7}$	-1.08×10^{-5}	4.68×10^{-3}	9.37×10^{-5}	3.25×10^{-5}	0.0054	7.27
217	<i>Planck</i> HFI	$7.79 \times 10^{-5} \pm 2.60 \times 10^{-6}$	-1.40×10^{-5}	2.09×10^{-2}	4.19×10^{-4}	4.51×10^{-5}	0.0054	5.01
353	<i>Planck</i> HFI	$2.76 \times 10^{-4} \pm 1.95 \times 10^{-5}$	-3.08×10^{-5}	9.32×10^{-2}	1.86×10^{-3}	1.51×10^{-4}	0.012	4.86
		Offset (MJy sr $^{-1}$)	Dipole (MJy sr $^{-1}$)	$s_{857,\nu}$	$\sigma_{s_{857,\nu}}$	n_ν (MJy sr $^{-1}$)		
545	<i>Planck</i> HFI	$7.27 \times 10^{-2} \pm 1.99 \times 10^{-2}$	1.63×10^{-2}	3.31×10^{-1}	6.62×10^{-3}	0.046	0.10	4.84
857	<i>Planck</i> HFI	$1.82 \times 10^{-2} \pm 6.02 \times 10^{-2}$...	1.0	2.0×10^{-2}	0.046	0.10	4.63
1250	DIRBE	$7.06 \times 10^{-2} \pm 1.19 \times 10^{-1}$...	1.98	3.97×10^{-2}	0.42	0.10	42
2141	DIRBE	$1.04 \times 10^{-1} \pm 1.54 \times 10^{-1}$...	2.56	5.12×10^{-2}	0.79	0.10	42
3000	DIRBE/IRAS	$0.0 \pm 4.3 \times 10^{-2}$...	1.27	2.53×10^{-2}	0.06	0.10	6.1

Notes. Column 1: approximate band center frequency of each input map. Note that 1250 GHz and 2141 GHz refer to the SFD reprocessings of DIRBE 240 μm and 140 μm , respectively. Column 2: instrument(s) from which the input map at each frequency has been obtained. Column 3: zero-level offset subtracted from each raw input map. Column 4: best-fit residual solar dipole amplitude according to Equation (3). Column 5: dimensionless correlation slope of each map relative to *Planck* 857 GHz. These are the correlation slopes used in the analysis of Section 6, specifically Equation (10). Column 6: adopted uncertainty on the dimensionless correlation slopes relative to *Planck* 857 GHz, for use in Equation (10). Column 7: n_ν represents the adopted per-pixel statistical noise level at full resolution, which contributes to the error budget of Equation (14). Column 8: multiplicative fractional uncertainty on each input map, for use in the error budget of Equation (14). Column 9: native angular resolution of each input map.

to thermal dust emission in *Planck* 143 GHz is ≥ 0.001 for only $< 2\%$ of the sky.

To correct for molecular emission, we employ the *Planck* Type 3 CO data product, which boasts the highest signal-to-noise ratio (S/N) among the available full-sky CO maps based on the *Planck* HFI and Low Frequency Instrument data (Planck Collaboration et al. 2013g). The native angular resolution of the Type 3 CO map is 5'. We therefore begin by smoothing the raw Type 3 CO map to match the PSF of the smoothed *Planck* intensity maps we wish to correct for molecular emission.

We must apply the appropriate unit conversions to the Type 3 CO map before subtracting it from the *Planck* intensity maps, which have native units of K_{CMB} at the frequencies of interest. The Type 3 CO map is provided in units of $K_{\text{RJ}} \text{ km s}^{-1}$ of $J = 1 \rightarrow 0$ emission. To convert this quantity to K_{CMB} , we assume that all of the CO emission arises from the ^{12}CO isotope, and derive the *Planck*-observed CO intensity in units of K_{CMB} as follows:

$$I_{\text{CO},\nu_i,N,N-1} = I_3 F_{12\text{CO},\nu_i,N,N-1} R_{N,N-1}, \quad (1)$$

where $I_{\text{CO},\nu_i,N,N-1}$ is the intensity in K_{CMB} in *Planck* band ν_i due to the CO transition from $J = N$ to $J = (N-1)$. I_3 represents the appropriately smoothed Type 3 CO amplitude in $K_{\text{RJ}} \text{ km s}^{-1}$ of $J = 1 \rightarrow 0$ emission. The $F_{12\text{CO},\nu_i,N,N-1}$ are conversion factors between $K_{\text{RJ}} \text{ km s}^{-1}$ and K_{CMB} for particular band/transition pairs. The relevant values, calculated with the *Unit Conversion and Colour Correction* software utilities (v1.2), are

$$F_{12\text{CO},100,1,0} = 1.478 \times 10^{-5} K_{\text{CMB}} / (K_{\text{RJ}} \text{ km s}^{-1}),$$

$$F_{12\text{CO},217,2,1} = 4.585 \times 10^{-5} K_{\text{CMB}} / (K_{\text{RJ}} \text{ km s}^{-1}),$$

and

$$F_{12\text{CO},353,3,2} = 1.751 \times 10^{-4} K_{\text{CMB}} / (K_{\text{RJ}} \text{ km s}^{-1}).$$

$R_{N,N-1}$ represents the line ratio of the transition from $J = N$ to $J = (N-1)$ relative to the $J = 1 \rightarrow 0$. Thus, $R_{1,0} = 1$, and we further adopt $R_{2,1} = 0.595$ and $R_{3,2} = 0.297$ based on Planck Collaboration et al. (2013g). These line ratios are assumed to be constant over the entire sky.

Formally, then, the CO contamination in band ν_i is given by

$$I_{\text{CO},\nu_i} = \sum_N I_{\text{CO},\nu_i,N,N-1}. \quad (2)$$

It happens that, for each of the *Planck* bands in which CO emission is non-negligible (100, 217, and 353 GHz), only a single N contributes ($N = 1$, $N = 2$, and $N = 3$, respectively).

Unfortunately, the Type 3 CO map at 6' FWHM is rather noisy, and the vast majority of the sky has completely negligible CO emission. Thus, in order to avoid adding unnecessary noise outside of molecular cloud complexes and at high latitudes, we have zeroed out low-signal regions of the Type 3 CO map. We identify low-signal regions as those with $\mathcal{I}_3 < 1 K_{\text{RJ}} \text{ km s}^{-1}$, where \mathcal{I}_3 is the Type 3 CO map smoothed to 0°25 FWHM. As a result of this cut, 90% of the sky remains unaffected by our CO correction, particularly the vast majority of the high Galactic latitude sky.

3.5. Zero Level

Although we wish to isolate and model thermal emission from Galactic dust, the *Planck* maps contain additional components on large angular scales. At each frequency, there can exist an overall, constant offset that must be subtracted to set the zero level of Galactic dust by removing the mean cosmic infrared background (CIB; Hauser & Dwek 2001), as well as any instrumental offset. Additionally, faint residuals of the solar dipole remain at low frequencies. We will address these issues by separately solving two sub-problems: first, we set the absolute zero level of *Planck* 857 GHz relative to external data, and second we fit the 100–545 GHz offsets and low-order corrections by correlating these *Planck* bands against *Planck* 857 GHz.

3.5.1. Absolute Zero Level

In Planck Collaboration et al. (2013a), the absolute zero level of thermal dust emission was set by requiring that *Planck* IR emission tends to zero when H_1 is zero, assuming a linear correlation between these two measurements at low column density. However, this approach is less than completely satisfying in that there appear to be different slopes of *Planck* 857 GHz versus H_1 for different ranges of H_1 intensity.

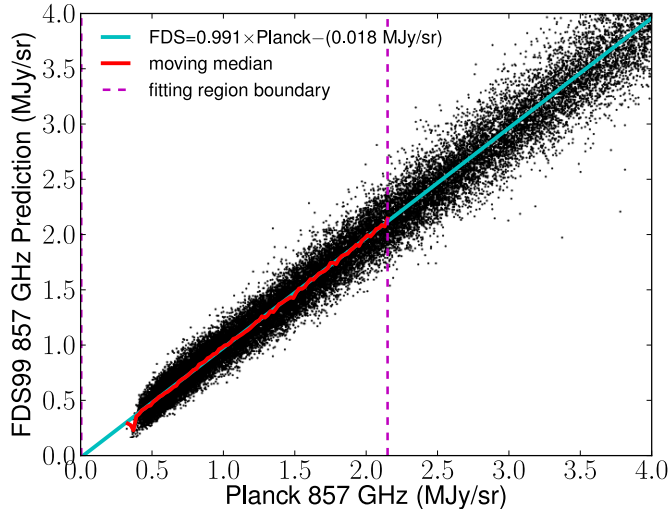


Figure 1. Scatter plot of **FDS99**-predicted 857 GHz thermal dust emission vs. *Planck* 857 GHz observations, illustrating our absolute zero-level determination described in Section 3.5.1.

In particular, *Planck* 857 GHz appears to “flatten out” at very low H_I, as shown in Figure 5 of Planck Collaboration et al. (2013a). More quantitatively, we have found, using the Leiden/Argentine/Bonn (LAB) Survey of Galactic H_I data (Kalberla et al. 2005) for $-72 < v_{\text{LSR}} < +25 \text{ km s}^{-1}$, that the best-fit slope for $\text{H}_I < 70 \text{ K km s}^{-1}$ is a factor of ~ 1.9 lower than the best-fit slope for $110 \text{ K km s}^{-1} < \text{H}_I < 200 \text{ K km s}^{-1}$, and as a result the implied zero-level offsets for *Planck* 857 GHz differ by $\sim 0.37 \text{ MJy sr}^{-1}$.

Because of this ambiguity in the relationship between 857 GHz and H_I emission, we decided to instead constrain the *Planck* 857 GHz zero level by comparison to the **FDS99**-predicted 857 GHz thermal dust emission. This renders our *Planck* 857 GHz absolute zero level tied indirectly to H_I through the **FDS99** 100 μm and 240 μm zero levels.

We perform a linear fit to the **FDS99**-predicted 857 GHz values as a function of *Planck* 857 GHz. For this purpose, we employ a version of the *Planck* 857 GHz map with zodiacal light and point sources removed and smoothed to 1° FWHM, which we will refer to as \mathcal{I}_{857} . We consider \mathcal{I}_{857} to be the independent variable, as it has much higher S/N than the **FDS99** prediction, henceforward referred to as \mathcal{F}_{857} . Note that \mathcal{F}_{857} is not simply the **FDS99** model evaluated at 857 GHz, but also incorporates the color correction factor of Section 5, using the **FDS99** temperature map to determine the dust spectrum shape. We rebin to $N_{\text{side}} = 64$ and restrict to pixels with $\mathcal{I}_{857} < 2.15 \text{ MJy sr}^{-1}$. Since *Planck* 857 GHz smoothed to degree resolution has very high S/N, we can safely perform such a cut on \mathcal{I}_{857} . Figure 1 shows a scatter plot of \mathcal{I}_{857} versus \mathcal{F}_{857} , with a moving median and linear fit overplotted. The linear fit was performed with uniform weights and iterative outlier rejection. The best-fit linear model is given by $\mathcal{F}_{857} = 0.991\mathcal{I}_{857} - 0.018 \text{ MJy sr}^{-1}$. It is encouraging that the slope is quite close to unity. It is also encouraging that our choice of *Planck* 857 GHz threshold at 2.15 MJy sr^{-1} is unimportant; any threshold value between 1.3 MJy sr^{-1} (28th percentile in \mathcal{I}_{857}) and 3.9 MJy sr^{-1} (61st percentile in \mathcal{I}_{857}) yields a zero-level offset within 0.01 MJy sr^{-1} of our adopted value.

The formal statistical error on the best-fit 857 GHz offset is quite small, $\sim 0.002 \text{ MJy sr}^{-1}$. The systematics likely to dominate the actual uncertainty on our FDS-based zero level are

imperfections in the *Planck*/i100 zodiacal light models and the **FDS99** temperature map. To quantify these systematic uncertainties, we split the sky into four quadrants, with boundaries at $b = 0^\circ$ and $l = 0^\circ, l = 180^\circ$. We again restricted to $\mathcal{I}_{857} < 2.15 \text{ MJy sr}^{-1}$, and repeated the regression in each quadrant. The rms of the per-quadrant slopes was found to be 0.0188, while the rms of the per-quadrant offsets was $0.0586 \text{ MJy sr}^{-1}$. Our adopted $\sim 0.06 \text{ MJy sr}^{-1}$ zero-level uncertainty is sufficiently large to be consistent with the possible error introduced by assuming no appreciable solar dipole signal in the *Planck* 857 GHz map. If we allow for a dipole template in our **FDS99** versus *Planck* linear regression at 857 GHz, the best-fit dipole amplitude is only 0.02 MJy sr^{-1} .

3.5.2. Relative Zero Level

In the course of this study we use not only *Planck* 857 GHz, but also all of the remaining *Planck* HFI bands, as well as i100. To derive the zero-level offsets that must be applied to each of the five lowest-frequency *Planck* bands, we perform a regression versus the *Planck* 857 GHz map corrected for the best-fit absolute zero-level offset from Section 3.5.1. We assume no offset need be applied to i100, which already has its zero level tied to H_I by SFD.

The need for additional low-order corrections beyond simple scalar offsets became evident upon inspecting the HFI maps at 100–545 GHz. In particular, we noticed the presence of a low-level dipole pattern, with an orientation consistent with that of the solar dipole. Our strategy will be to simultaneously fit both this residual dipole and the zero-level offset amplitude for each band. To most precisely recover these amplitudes, it is necessary to have the highest available S/N in the independent variable of our regression. For this reason we have used *Planck* 857 GHz as a reference for the 100–545 GHz bands, as opposed to the **FDS99** predictions or H_I data. In doing so, we assume *Planck* 857 GHz contains no appreciable solar dipole residual.

We perform one regression per HFI band (other than 857 GHz) to simultaneously fit for the zero-level offset, the slope relative to 857 GHz, and the residual dipole amplitude. For each 100–545 GHz HFI band, we restrict to regions of low column density ($\text{H}_I < 200 \text{ K km s}^{-1}$ for $-72 < v_{\text{LSR}} < +25 \text{ km s}^{-1}$) and fit the following model:

$$\mathcal{I}_{v_i,p} = m\mathcal{I}_{857,p} + b + d\mathcal{D}_p. \quad (3)$$

With p denoting a single $N_{\text{side}} = 64$ HEALPix pixel (Górski et al. 2005) in the maps \mathcal{I}_{857} , \mathcal{I}_{v_i} , and \mathcal{D} . Here \mathcal{I}_{857} is the *Planck* 857 GHz map with zodiacal emission, compact sources, and the constant offset of Section 3.5.1 removed, smoothed to 1° resolution. \mathcal{I}_{v_i} is the corresponding 1° resolution *Planck* HFI map with zodiacal emission, CMB anisotropies, and compact sources removed. In the context of Equation (3), $v_i \in \{100, 143, 217, 353, 545\} \text{ GHz}$. Note that \mathcal{I}_{v_i} is always in the native units of the relevant *Planck* band. \mathcal{D} is a scaling of the solar dipole pattern oriented toward $(l, b) = (263^\circ 99, 48^\circ 26)$, with unit amplitude. Because $\sim 18,000$ pixels satisfy the low H_I cut, we have an overconstrained linear model with three parameters: m , d , and b . m represents the best-fit slope of *Planck* band v_i versus *Planck* 857 GHz assuming they are linearly related. d is the residual solar dipole amplitude, and its best-fit value represents the scaling of the solar dipole that makes the *Planck* band v_i versus 857 GHz correlation most tightly linear. b represents the constant offset that must be subtracted from the band v_i map to make its zero level consistent with that of the 857 GHz map. For

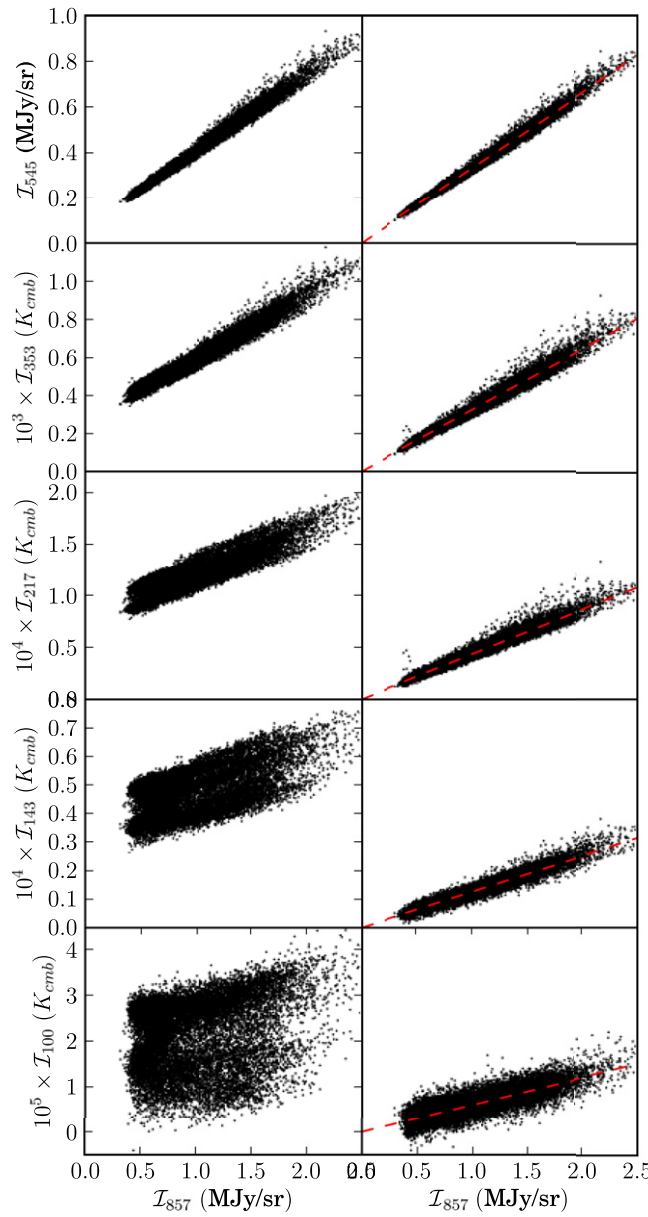


Figure 2. Scatter plots of *Planck* 100, 143, 217, 353, and 545 GHz vs. *Planck* 857 GHz. Left: before applying our best-fit zero-level offsets and additional low-order corrections. Right (top four panels): *Planck* 143–545 GHz after correcting for each band’s best-fit offset and residual solar dipole. Bottom right: *Planck* 100 GHz after applying the spherical harmonic corrections of Equation (4). The dashed red line shows the best-fit linear relationship in all cases.

each band ν_i , we obtain estimates of m , d , and b by performing a linear least-squares fit with uniform weights and iterative outlier rejection. Figure 2 shows scatter plots of the band ν_i versus 857 GHz correlation before (left) and after (right) correcting for the best-fit offset and residual dipole, for each $\nu_i \in \{143, 217, 353, 545\}$ GHz. Not only are the tightened correlations striking in these scatter plots, but the residual dipole subtractions appear very successful in the two-dimensional band ν_i maps themselves. Before performing thermal dust fits, we therefore subtract the best-fit b and dD from each 143–545 GHz map. The best-fit offsets and residual dipole amplitudes are listed in Table 1, along with other important per-band parameters, such as the fractional multiplicative calibration uncertainty c_v .

We found that a dipole correction alone could not sufficiently rectify the *Planck* 100 GHz map (see Figure 3). Therefore, for

100 GHz, we performed a modified version of the Equation (3) fit, using the following model:

$$\mathcal{I}_{100,p} = m\mathcal{I}_{857,p} + b + \sum_{l=1}^4 \sum_{m=-l}^l a_{lm} Y_l^m(\theta_p, \phi_p), \quad (4)$$

where Y_l^m are the real spherical harmonics, and the a_{lm} are their corresponding real coefficients. The angle ϕ_p is taken simply to be $l_{\text{gal},p}$ and $\theta_p = (90^\circ - b_{\text{gal},p})$. Thus, we have replaced the solar dipole term with a sum of 24 spherical harmonic templates, which, when multiplied by the best-fit a_{lm} coefficients and subtracted from *Planck* 100 GHz make the relation between 100 GHz and 857 GHz most tightly linear. Figure 3 illustrates the improved correlation of 100 GHz versus 857 GHz when including the spherical harmonic corrections relative to the dipole-only correction. The spherical harmonic decomposition of Equation (4) did not improve the correlations at higher frequencies enough to warrant replacing the dipole-only correction in those cases.

4. DUST EMISSION MODEL

At sufficiently high frequencies, Galactic thermal dust emission can be adequately modeled as a single MBB with power-law emissivity (e.g., SFD; Planck Collaboration et al. 2013a). However, it has long been recognized, particularly in view of the FIRAS spectra, that the dust SED flattens toward the millimeter in a manner that is not consistent with a simple extrapolation of single-MBB models to low frequencies. In the diffuse ISM, Reach et al. (1995) found an improved fit to the FIRAS data using an empirically motivated superposition of two $\beta = 2$ MBBs, one representing a “hot” grain population ($T \approx 16$ –21 K), the other a “cold” grain population ($T \approx 4$ –7 K). FDS99 built a more physically motivated two-MBB model, in which different grain emission/absorption properties account for the differing temperatures of each population, and these temperatures are coupled by assuming thermal equilibrium with the same interstellar radiation field (ISRF).

The primary FDS99 analysis considered the intrinsic grain properties of each species, for example, the emissivity power-law indices, to be constant over the sky, and performed a correlation slope analysis to constrain these parameters with FIRAS and DIRBE observations. FDS99 also constructed a DIRBE 240 μm /100 μm ratio to account for temperature variation at ~ 1.3 resolution. In this work we seek to apply the FDS99 emission model to the *Planck* data set, which offers a dramatic enhancement in angular resolution relative to the FIRAS spectra. The *Planck* data thereby allow us to derive an improved temperature correction at near-IRAS resolution (Section 7.3), re-evaluate the best-fit global dust properties (Sections 6 and 7.5), and fit additional two-component model parameters as a function of position on the sky (Section 7.4).

The shape of the two-component model spectrum we will consider is given by

$$M_\nu \propto \left[f_1 q_1 \left(\frac{\nu}{\nu_0} \right)^{\beta_1} B_\nu(T_1) + f_2 q_2 \left(\frac{\nu}{\nu_0} \right)^{\beta_2} B_\nu(T_2) \right], \quad (5)$$

where B_ν is the Planck function, T_1 is the “cold” dust temperature, T_2 is the “hot” dust temperature, and β_1 and β_2 are the emissivity power-law indices of the cold and hot dust components, respectively. q_1 represents the ratio of FIR emission cross section to optical absorption cross section for species 1,

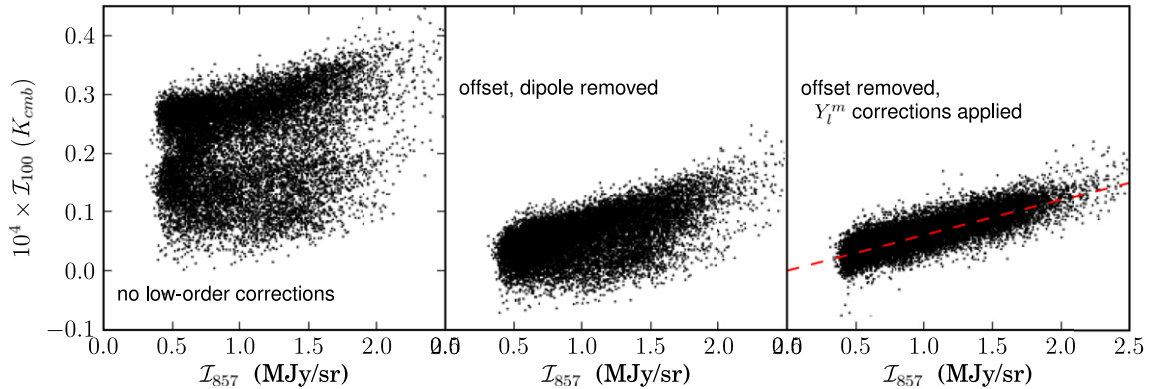


Figure 3. Summary of low-order corrections at 100 GHz. Left: prior to our low-order corrections, a $\sim 17 \mu\text{K}$ zero-level offset is present and strong low-order problems reduce the linearity of the 100 GHz trend vs. 857 GHz. Center: scatter plot of *Planck* 100 GHz vs. 857 GHz after applying the best-fit offset and residual solar dipole corrections derived with Equation (3) to *Planck* 100 GHz. The correlation is strengthened, but remains far less tight than for 143–545 GHz (see the right column of Figure 2, top four rows). Right: after applying the spherical harmonic corrections of Equation (4) to *Planck* 100 GHz, the correlation vs. 857 GHz is far more tightly linear than following the dipole correction.

Table 2
Global Model Parameters

Number	Model	f_1	q_1/q_2	β_1	β_2	T_2	T_1	n	dof	χ^2	χ_v^2
1	FDS99 best-fit	0.0363	13.0	1.67	2.70	15.72	9.15	1.018	7	23.9	3.41
2	FDS99 general	0.0485	8.22	1.63	2.82	15.70	9.75	0.980	3	3.99	1.33
3	Single MBB	0.0	1.59	19.63	...	0.999	6	33.9	5.65

and similarly q_2 for species 2. f_1 and f_2 dictate the relative contributions of the two-MBB components to the combined SED. Thus, f_1 and f_2 can be thought of as encoding the mass fraction of each species, although technically f_1 (f_2) is the optical absorption cross-section weighted mass fraction for species 1 (2). Following the convention of FDS99, we choose $\nu_0 = 3000$ GHz and take $f_2 = (1 - f_1)$.

Mathematically, this two-MBB model requires specification of seven parameters for every line of sight: T_1 , T_2 , β_1 , β_2 , f_1 , q_1/q_2 , and the normalization of M_ν . However, under the assumption that the temperature of each species is determined by maintaining thermal equilibrium with the same ISRF, $T_1 = T_1(T_2, \beta_1, \beta_2, q_1/q_2)$ is fully determined by these other parameters. T_1 is always related to T_2 via a simple power law, although the prefactor and exponent depend on the parameters q_1/q_2 , β_1 and β_2 (see FDS99, Equation (14)).

These considerations still leave us with six potentially free parameters per line of sight. Unfortunately, fitting this many parameters per spatial pixel is not feasible for our full-resolution 6° fits, as these are constrained by only five broadband intensity measurements. Hence, as in FDS99, we deem certain parameters to be “global,” i.e., spatially constant over the entire sky. In our full-resolution five-band fits, we designate β_1 , β_2 , f_1 , and q_1/q_2 to be spatially constant. This same approach was employed by FDS99, and the globally best-fit values obtained by FDS99 for these parameters are listed in the first row of Table 2. With these global parameters, FDS99 found $T_2 \approx 16.2$ K, $T_1 \approx 9.4$ K to be typical at high latitude. In Section 6, we discuss the best-fit global parameters favored by the *Planck* HFI data; these are listed in the second row of Table 2.

Fixing the aforementioned four global parameters, our full-resolution, five-band fits have two remaining free parameters per line of sight: the hot dust temperature T_2 determines the SED shape and the normalization of M_ν determines the SED amplitude. In the lower-resolution fits of Section 7.4, which include all HFI bands, we will allow f_1 to be a third free parameter, still holding β_1 , β_2 , and q_1/q_2 fixed.

To calculate the optical depth in the context of this model, we assume optically thin conditions, meaning that $\tau_\nu = M_\nu/S_\nu$, where M_ν is the appropriately scaled two-component model intensity and the source function is given by:

$$S_\nu = \frac{f_1 q_1 (\nu/\nu_0)^{\beta_1} B_\nu(T_1) + f_2 q_2 (\nu/\nu_0)^{\beta_2} B_\nu(T_2)}{f_1 q_1 (\nu/\nu_0)^{\beta_1} + f_2 q_2 (\nu/\nu_0)^{\beta_2}}. \quad (6)$$

5. PREDICTING THE OBSERVED SED

The thermal dust emission model of Section 4 predicts the flux density per solid angle M_ν in, e.g., MJy sr⁻¹ for any single frequency ν . In practice, however, we wish to constrain our model using measurements in the broad *Planck*/DIRBE bandpasses, each with $\Delta\nu/\nu \sim 0.3$. Both the *Planck* and DIRBE data products quote flux density per solid angle in MJy sr⁻¹ under the “IRAS convention.” More precisely, each value reported in the *Planck* maps gives the amplitude of a power-law spectrum with $\alpha = -1$, evaluated at the nominal band center frequency, such that this spectrum integrated against the transmission reproduces the bolometer-measured power. Because our model spectra do not conform to the $\alpha = -1$ convention, we have computed color correction factors to account for the MBB (T , β) spectral shape and the transmission as a function of frequency:

$$b_{\nu_i}(T, \beta) = \frac{\int \nu^\beta B_\nu(T) T_{\nu_i}(\nu) d\nu [\int (\nu_{i,c}/\nu) T_{\nu_i}(\nu) d\nu]^{-1}}{\nu_{i,c}^\beta B_{\nu_{i,c}}(T)}. \quad (7)$$

Here $\nu_{i,c}$ is the nominal band center frequency of band ν_i , with $\nu_{i,c} \in \{100, 143, 217, 353, 545, 857, 1249, 1352, 2141, 3747, 2997, 92458\}$ GHz. $T_{\nu_i}(\nu)$ represents the relative transmission as a function of frequency for band ν_i . For the HFI maps, $T_{\nu_i}(\nu)$ is given by the *Planck* transmission curves provided in the file HFI_RIMO_R1.10.fits (Planck Collaboration et al. 2013c). For i100 and DIRBE 140 μm , 240 μm , we have adopted the corresponding DIRBE transmission curves.

The two-component model prediction in band ν_i under the *IRAS* convention, termed \tilde{I}_{ν_i} , is then constructed as a linear combination of color-corrected MBB terms:

$$\tilde{I}_{\nu_i} \propto \sum_{k=1}^2 b_{\nu_i}(T_k, \beta_k) f_k q_k (\nu_{i,c}/\nu_0)^{\beta_k} B_{\nu_{i,c}}(T_k). \quad (8)$$

The color correction of Equation (7) therefore allows us to predict \tilde{I}_{ν_i} by computing monochromatic flux densities at the central frequency $\nu_{i,c}$ and then multiplying by factors $b_{\nu_i}(T, \beta)$. In practice, we interpolated the color corrections off of a set of precomputed, one-dimensional lookup tables each listing $b_{\nu_i}(T, \beta)$ for a single β value as a function of T . We thus avoided the need to interpolate in both β and T by computing only a small set of one-dimensional correction factors for the particular set of β values of interest (e.g., $\beta = 1.67, 2.7, 1.63, 2.82, \dots$, see Table 2). This color correction approach makes the MCMC sampling described in Section 7.3 much more computationally efficient by circumventing the need to perform the integral in the numerator of Equation (7) on-the-fly for each proposed dust temperature. We have chosen to compute the color corrections on a per-MBB basis because this approach is very versatile; all possible two-component (and single-MBB) models are linear combinations of MBBs, so we can apply all of our color correction machinery even when we allow parameters other than temperature (e.g., f_1) to vary and thereby modify the dust spectrum shape.

With these color corrections and the formalism established in Section 4 in hand, we can mathematically state the model we will use, e.g., during MCMC sampling to predict the observed SED. The predicted observation in band ν_i is given by

$$\tilde{I}_{\nu_i} = \frac{\sum_{k=1}^2 b_{\nu_i}(T_k, \beta_k) f_k q_k (\nu_{i,c}/\nu_0)^{\beta_k} B_{\nu_{i,c}}(T_k) u_{\nu_i}^{-1}}{\sum_{k=1}^2 b_{545}(T_k, \beta_k) f_k q_k (545 \text{ GHz}/\nu_0)^{\beta_k} B_{545}(T_k)} \tilde{I}_{545}. \quad (9)$$

This equation is quite similar to Equation (8), but with two important differences. First, the normalization of \tilde{I}_{ν_i} is now specified by \tilde{I}_{545} , which represents the *IRAS* convention *Planck* 545 GHz intensity. The denominator serves to ensure that, for the case of $\nu_i = 545$ GHz, \tilde{I}_{545} is self-consistent. Second, each term in the numerator is multiplied by a unit conversion factor $u_{\nu_i}^{-1}$. This factor is necessary because some of the *Planck* maps of interest have units of K_{CMB} (100–353 GHz), while the remaining maps (545–3000 GHz) have units of MJy sr⁻¹. We have adopted the strategy of predicting each band in its native units, whether MJy sr⁻¹ or K_{CMB} . For this reason, we always evaluate $B_{\nu_{i,c}}$ in Equation (9) in MJy sr⁻¹ and let $u_{\nu_i} = 1$ (dimensionless) for $\nu_i \geq 545$ GHz. For $\nu_i \leq 353$ GHz, u_{ν_i} represents the conversion factor from K_{CMB} to MJy sr⁻¹, given by (Planck Collaboration et al. 2013c, Equation (32)).

6. GLOBAL MODEL PARAMETERS

While we ultimately aim to obtain *Planck*-resolution maps of the spatially varying dust temperature and optical depth, we start by applying the machinery/formalism thus far developed to reassess the best-fit global two-component model parameters in light of the *Planck* HFI data.

FDS99 determined the best-fit values of the two-component model global parameters β_1 , β_2 , q_1/q_2 , and f_1 via a correlation

slope analysis incorporating DIRBE and FIRAS data. Here we seek to estimate these same global parameters via an analogous correlation slope analysis in which we swap the *Planck* HFI maps for FIRAS at low frequencies, while still relying on DIRBE at higher frequencies. We also seek to determine via this correlation slope analysis whether or not the combination of *Planck*+DIRBE data favors two-component models over single-MBB models in the same way that the FIRAS+DIRBE data did in the FDS99 analysis.

In the two-component model case, based on a spectrum of *Planck* and DIRBE correlations slopes, we wish to obtain estimates for six free parameters: β_1 , β_2 , q_1/q_2 , f_1 , T_2 , and the overall spectrum normalization n . The constraints we employ are the correlation slopes of each of the *Planck* HFI bands, as well as DIRBE 100 μm (3000 GHz), 140 μm (2141 GHz), and 240 μm (1250 GHz) relative to *Planck* 857 GHz, i.e., dI_{ν_i}/dI_{857} . We will refer to the slope for band ν_i relative to *Planck* 857 GHz as s_{857,ν_i} . The slopes for *Planck* 100–545 GHz are taken to be those derived from the relative zero-level fits of Section 3.5.2, and are illustrated by the dashed red lines in the right-hand column plots of Figure 2. The 857 GHz slope is unity by definition.

At 1250, 2141, and 3000 GHz, we use the SFD-reprocessed DIRBE maps. For each DIRBE band, we determine s_{857,ν_i} by performing a linear fit to DIRBE as a function of *Planck* 857 GHz, after both have been zodiacal light subtracted and smoothed to 1° FWHM, also restricting to the low H I mask of Section 3.5.2 (see Figure 4).

Counting 857 GHz, we thus have nine correlation slope constraints for six free parameters. Including DIRBE 140 μm and 240 μm is critical in making the problem at hand sufficiently overconstrained, and also in providing information near the peak of the dust SED at $\sim 160 \mu\text{m}$, which is particularly sensitive to the presence of a single versus multiple MBB components.

We assume an uncertainty of 2% on each of the s_{857,ν_i} and minimize the chi-squared given by

$$\chi^2 = \sum_{i=0}^8 \left[\frac{s_{857,\nu_i} - n \frac{\tilde{I}_{\nu_i}(\beta_1, \beta_2, f_1, q_1/q_2, T_2)}{\tilde{I}_{857}(\beta_1, \beta_2, f_1, q_1/q_2, T_2)}}{\sigma_{s_{857,\nu_i}}} \right]^2, \quad (10)$$

where $\nu_i \in \{100, 143, 217, 353, 545, 857, 1250, 2141, 3000\}$ GHz. Note that this formula encompasses the general two-component case; in the single-MBB case, we take $f_1 = 0$ and hence q_1/q_2 , β_1 , and T_2 are immaterial, but Equation (10) still applies. Note also that no “priors” are included to preferentially drag our results toward agreement with those of FDS99. The correlation slopes s_{857,ν_i} and their adopted uncertainties are listed in the fifth and sixth columns of Table 1.

The results of our chi-squared minimization are listed in Table 2. First (model 1), we fix β_1 , β_2 , q_1/q_2 , and f_1 to the best-fit values from the FDS99 analysis based on DIRBE+FIRAS. We then allow n and T_2 to vary so as to best match our DIRBE+*Planck* spectrum. This results in a reduced chi-squared of $\chi^2_v = 3.41$. Reassuringly, n is quite close to unity. It should be noted though that our best-fit T_2 is ~ 0.5 K lower than that found by FDS99 for the same values of β_1 , β_2 , q_1/q_2 , and f_1 .

Next (model 2), we consider the fully general two-component model, allowing all six model parameters to vary. In this case, the reduced chi-squared of the best-fit parameters is $\chi^2_v = 1.33$, signifying that our introduction of four additional free parameters is justified. The best-fit β_1 and β_2 are both consistent with the corresponding FDS99 values to within 5%. $q_1/q_2 = 8.22$ represents a $\sim 40\%$ lower value than found by FDS99, while

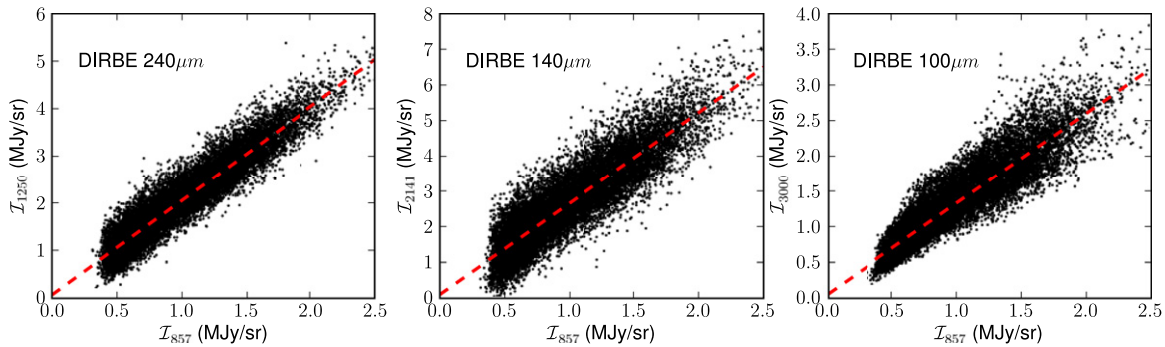


Figure 4. Linear fits of SFD-reprocessed DIRBE 240 μm (left), 140 μm (center), and 100 μm (right) as a function of *Planck* 857 GHz. The red lines illustrate the DIRBE correlation slopes used in our dust emission model optimization of Section 6.

$f_1 = 0.0458$ represents a $\sim 25\%$ increase relative to FDS99. Again, our best-fit high latitude T_2 is ~ 0.5 K lower than the typical value of $\langle T_2 \rangle = 16.2$ K from FDS99.

Lastly, we calculate the optimal single-MBB fit to the *Planck*+DIRBE correlation slope spectrum. The best-fit single MBB has $\beta = 1.59$, $T = 19.63$, and $\chi^2_v = 5.65$, indicating a significantly worse fit to the data than our best-fit two-component model (model 2). Thus, our *Planck*+DIRBE correlation slope analysis has confirmed the main conclusion of FDS99 and others, e.g., Reach et al. (1995), that the FIR/submm dust SED prefers two MBBs to just one, but, for the first time, independent of FIRAS. Still, it is apparent that the improvement in χ^2_v for single-MBB versus double-MBB models found here is substantially less dramatic ($\Delta\chi^2_v = 4.32$) than that found in FDS99 ($\Delta\chi^2_v = 29.2$). This is likely attributable to the exquisite narrow-band frequency coverage of FIRAS, especially near the dust SED peak, which makes FIRAS a better suited data set than *Planck* for a detailed analysis of the globally best-fit dust SED model. In Section 7.5, we confirm the basic conclusions of this section via an approach in which we allow the dust temperature to vary spatially. The analysis of Section 7.5 also allows us to confirm the conclusions of this section while including a fully detailed uncertainty model; our assumption of 2% per-band uncertainties on the correlation slopes is largely a statement that we seek a model accurate to 2% from 100–3000 GHz, although the fact that our χ^2_v values are order unity suggests that the assumed uncertainties are not grossly over or underestimated.

7. MCMC FITTING PROCEDURE

The following subsections detail our procedure for constraining the two-component dust emission model parameters which are permitted to vary spatially. We use the MCMC procedure described to perform two types of fits: (1) full-resolution 6'1 fits, in which only the SED normalization and dust temperatures vary spatially, and (2) lower-resolution fits in which f_1 is also allowed to vary from one line of sight to another.

7.1. Pixelization

For the purpose of fitting, we divide the sky into ~ 50 million pixels of angular size $\sim 1.72'$, defined by the HEALPix pixelization in Galactic coordinates, with $N_{\text{side}} = 2048$. This pixelization is convenient because it is the format in which the *Planck* HFI maps were released, and because it adequately samples the 6'1 FWHM maps under consideration in our full-resolution fits. Our procedure will fit the intensity measurements in each spatial pixel independently.

7.2. Sampling Parameters

As discussed in Section 4, our full-resolution fits consider the “global” parameters f_1 , q_1/q_2 , β_1 , β_2 to be spatially constant. We employ the best-fit *Planck*+DIRBE global parameters of Table 2, model 2. For each line of sight, only the dust spectrum normalization and dust temperatures are allowed to vary. In order to predict the dust SED for a given pixel, we are thus left with two remaining degrees of freedom (dof), and must choose an appropriate set of two parameters to sample and thereby constrain via MCMC. To determine the SED normalization in each pixel, we draw samples in \tilde{I}_{545} , the “IRAS convention” intensity in the *Planck* 545 GHz bandpass, as defined in Equation (9). With the four aforementioned global parameters fixed, the dust spectrum shape is determined entirely by the two dust temperatures, which are coupled. To constrain the dust temperatures, we sample in T_2 , the hot dust temperature. For each sample in T_2 , we compute the corresponding value of T_1 , thereby fully specifying the SED shape. In principle, we could sample in either T_1 or T_2 , but have chosen to sample in T_2 because emission from this component dominates in the relatively high frequency bands that most strongly constrain the dust temperatures.

For the lower-resolution fits described in Section 7.4, we sample in three parameters: \tilde{I}_{545} , T_2 , and f_1 .

7.3. Markov Chains

In our full-resolution fits, we use a MCMC approach to constrain the parameters \tilde{I}_{545} and T_2 . For each pixel, we run a Metropolis–Hastings (MH) Markov chain sampling the posterior probability of the observed 217–3000 GHz thermal dust SED as a function of the two parameters \tilde{I}_{545} and T_2 . More specifically, for each pixel, we are sampling the posterior given by

$$P(\tilde{I}_{545}, T_2 | \mathbf{I}) \propto \mathcal{L}(\mathbf{I} | \tilde{I}_{545}, T_2) P(T_2) P(\tilde{I}_{545}). \quad (11)$$

Here \mathbf{I} denotes the vector of observed thermal dust intensities quoted under the “IRAS convention”: $\mathbf{I} = (I_{217}, I_{353}, I_{545}, I_{857}, I_{3000})$. The likelihood function is given by

$$\mathcal{L}(\mathbf{I} | \tilde{I}_{545}, T_2) = \exp \left[-\frac{1}{2} (\mathbf{I} - \tilde{\mathbf{I}})^T \Sigma^{-1} (\mathbf{I} - \tilde{\mathbf{I}}) \right]. \quad (12)$$

Here $\tilde{\mathbf{I}}$ is the vector of predicted observations based on Equation (9) and the proposed values of \tilde{I}_{545} and T_2 : $\tilde{\mathbf{I}} = (\tilde{I}_{217}, \tilde{I}_{353}, \tilde{I}_{545}, \tilde{I}_{857}, \tilde{I}_{3000})$. Σ is the per-pixel covariance matrix constructed based on the uncertainties in the observed intensities:

$$\Sigma = \begin{pmatrix} \sigma_{217}^2 & \dots & \rho_{217,3000}\sigma_{217}\sigma_{3000} \\ \vdots & \ddots & \vdots \\ \rho_{3000,217}\sigma_{3000}\sigma_{217} & \dots & \sigma_{3000}^2 \end{pmatrix}. \quad (13)$$

For each pixel p in band ν_i , the variance of the measured value $I_{\nu_i}(p)$ is taken to be

$$\sigma_{\nu_i}^2(p) = c_{\nu_i}^2 I_{\nu_i}^2(p) + c_{\nu_i}^2 \sigma_{\text{CMB}, \nu_i}^2 + (\delta O_{\nu_i})^2 + n_{\nu_i}^2 + \sigma_{\text{CO}, \nu_i}^2(p) + \sigma_{\text{CIBA}, \nu_i}^2. \quad (14)$$

This error budget is modeled after (Planck Collaboration et al. 2013a; Equation (B1)), but with some modifications and additions. The first term accounts for the multiplicative uncertainty on the input maps. Table 1 lists the multiplicative calibration uncertainty c_ν for each band. These values are taken from Table 11 of Planck Collaboration et al. (2013e). The second term represents an uncertainty due to our subtraction of the SMICA CMB model. The analogous term in (Planck Collaboration et al. 2013a, Equation (B1)) is $(c_\nu \times \text{SMICA}(p))^2$, i.e., an uncertainty proportional to the CMB model amplitude in each pixel. Because this term's spatial dependence can imprint the CMB anisotropies on the derived parameters, we have chosen to replace $\text{SMICA}(p)$ with a spatially constant, rms value for the CMB amplitude, $\sigma_{\text{CMB}, \nu_i}$. δO_{ν_i} represents the uncertainty in the band ν_i zero-level offset, and the values of δO_{ν_i} can be read off from the second column of Table 1. n_{ν_i} represents the instrumental noise in band ν_i . Because using per-pixel noise estimates based on the *Planck* ii_cov parameter can imprint features of the survey pattern onto the derived parameters, we have adopted a conservative, spatially constant value of n_{ν_i} for each band. These values of n_{ν_i} are listed in Table 1. The next term accounts for the uncertainty on the CO emission correction, taking $\sigma_{\text{CO}, \nu_i}(p) = 0.15 \times I_{\text{CO}, \nu_i}(p)$ (see Section 3.4, specifically Equation (2)).

Finally, we include a term to account for the rms amplitude of the cosmic infrared background anisotropy (CIBA) in band ν_i , $\sigma_{\text{CIBA}, \nu_i}$. The values for the CIBA rms amplitudes are obtained by assuming a $T = 18.3$ K, $\beta = 1.0$ MBB spectrum for the CIB, with 857 GHz normalization from Planck Collaboration et al. (2011b). The CIBA not only contributes to the per-band variance $\sigma_{\nu_i}^2$, but also to the inter-frequency covariances; this is why we have included the off-diagonal terms in the covariance matrix of Equation (13). In our noise model, the CIBA is the only source of inter-frequency covariance. Thus, the off-diagonal covariance matrix element between bands ν_i and ν_j is given by

$$\Sigma_{ij} = \rho_{\nu_i, \nu_j} \sigma_{\nu_i} \sigma_{\nu_j} = \rho_{\text{CIBA}, \nu_i, \nu_j} \sigma_{\text{CIBA}, \nu_i} \sigma_{\text{CIBA}, \nu_j}, \quad (15)$$

with values for $\rho_{\text{CIBA}, \nu_i, \nu_j}$ from Planck Collaboration et al. (2013i). The approach we have taken in accounting for the CIBA is similar to that of Planck Collaboration et al. (2013a), Appendix C, in that we treat the CIBA amplitude in each pixel as a Gaussian random draw. However, instead of performing a separate analysis to gauge the uncertainty on derived dust parameters due to the CIBA, we allow the CIBA covariance to propagate naturally into our uncertainties via the likelihood function. Still, our treatment of the CIBA is a major oversimplification; a more sophisticated approach that accounts for the detailed CIBA spatial structure, or even removes the CIBA by subtraction would be preferable.

We include the following prior on the hot dust temperature:

$$P(T_2) = \mathcal{N}(T_2 | \bar{T}_2, \sigma_{\bar{T}_2}), \quad (16)$$

with $\bar{T}_2 = 15.7$ K and $\sigma_{\bar{T}_2} = 1.4$ K. The T_2 prior mean is chosen based on the typical high-latitude T_2 value derived from the correlation slope analysis of Section 6. We find, as desired, that this relatively broad T_2 prior has little influence on the derived temperatures, other than to regularize the rare pixels with one or more defective intensities, which might otherwise yield unreasonable parameter estimates. In principle, there can also be an informative prior on \tilde{I}_{545} . However, we have chosen to assume a uniform prior on the SED normalization and, as a matter of notation, will omit $P(\tilde{I}_{545})$ henceforward. In practice we always perform computations using logarithms of the relevant probabilities.

For each pixel, we initialize the Markov chain with parameters $\tilde{I}_{545} = I_{545}$ and T_2 consistent with the FDS99 DIRBE 100 $\mu\text{m}/240 \mu\text{m}$ ratio map \mathcal{R} . The initial proposal distribution is a two-dimensional normal distribution, with $\sigma_{T_2} = 0.25$ K, $\sigma_{\tilde{I}_{545}} = \max(0.01 \times I_{545}, 0.05 \text{ MJy sr}^{-1})$ and $\rho_{T_2, \tilde{I}_{545}} = 0$. We run five iterations of burn-in, each consisting of 500 MH steps. After each burn-in iteration, we rescale the proposal distribution so as to ultimately attain an acceptance fraction f_{acc} as close as possible to the optimal value $f_{\text{opt}} = 0.234$. This is accomplished by multiplying the proposal distribution standard deviations by $f_{\text{acc}}/f_{\text{opt}}$.

After burn-in, we estimate the parameters and their uncertainties by performing 10,000 sampling steps, with $T_{2,j}$ and $\tilde{I}_{545,j}$ denoting the proposed parameter values at the j th step since the end of burn-in. From these 10,000 samples, we compute estimates of each parameter's mean, $\langle T_2 \rangle = \langle T_{2,j} \rangle$, $\langle \tilde{I}_{545} \rangle = \langle \tilde{I}_{545,j} \rangle$, of each parameter's variance, $\sigma_{T_2}^2 = \langle T_{2,j}^2 \rangle - \langle T_{2,j} \rangle^2$, $\sigma_{\tilde{I}_{545}}^2 = \langle \tilde{I}_{545,j}^2 \rangle - \langle \tilde{I}_{545,j} \rangle^2$, and of the covariance $\sigma_{T_2} \sigma_{\tilde{I}_{545}} = \langle T_{2,j} - \langle T_{2,j} \rangle \rangle \langle \tilde{I}_{545,j} - \langle \tilde{I}_{545,j} \rangle \rangle$.

After obtaining this initial estimate of the covariance matrix for each pixel, we re-run a second iteration of the entire MCMC procedure, starting from the first burn-in period. On this iteration, for each pixel, we begin with a proposal distribution that is a two-dimensional Gaussian with covariance equal to the first-pass covariance estimate. This gives the each pixel's proposal distribution approximately the "right shape," whereas on the first pass we started by simply guessing the relative widths of the proposal distribution in \tilde{I}_{545} , T_2 , and also assumed that the $\rho_{T_2, \tilde{I}_{545}} = 0$.

Lastly, during post burn-in sampling, we also estimate the monochromatic two-component intensity at 545 GHz, $M_{545} = \langle M_{545,j} \rangle = \langle \tilde{I}_{545,j} / b_{545}(T_{2,j}, \beta_2) \rangle$, its variance, and the 545 GHz optical depth $\tau_{545} = \langle \tau_{545,j} \rangle = \langle M_{545,j} / S_{545,j} \rangle$ and its variance. τ_{545} and M_{545} are more readily useful than the sampling parameters themselves for translating our fit results into predictions of reddening (Section 8) and thermal dust emission (Section 9.2), respectively. At high Galactic latitude, we find a typical T_2 uncertainty of 0.45 K, and typical \tilde{I}_{545} fractional uncertainty of 13%. Figure 5 illustrates the two-component model SED and the intensity measurements that constrain our fits, while Figure 6 shows example posterior probability density functions (PDFs) for three pixels. Figure 7 shows a map of our derived hot dust temperature at full resolution, for a patch of sky in the Polaris flare region.

We validated the parameters and uncertainties recovered from our MCMC procedure by comparing with results based on finely gridded posterior calculations performed on a random subset of pixels. These comparisons verified that the proposal distribution rescaling and reshaping steps that we employ do improve the

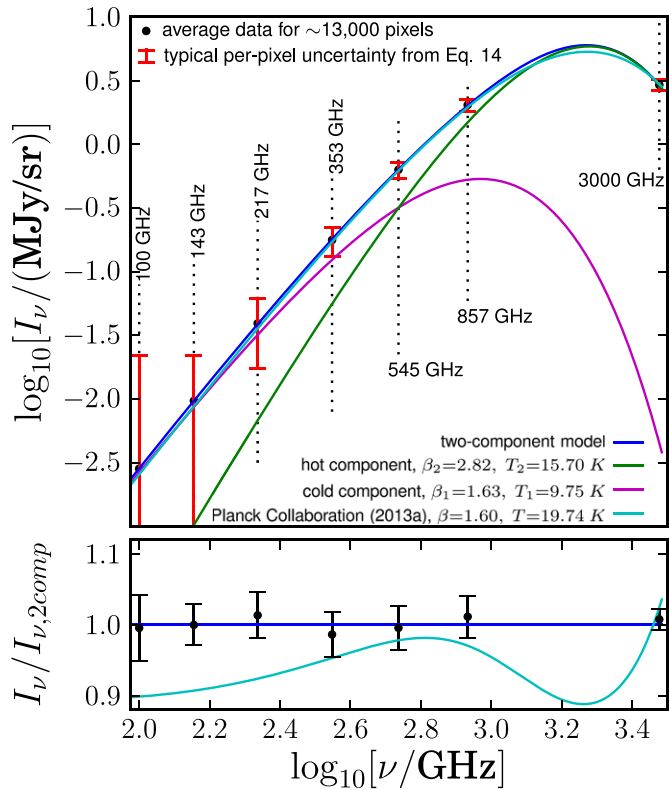


Figure 5. Top: summary of observed SEDs and best-fit thermal dust emission models for $\sim 13,000 N_{\text{side}} = 2048$ pixels with similar best-fit temperatures and optical depths ($15.695 \text{ K} < T_2 < 15.705 \text{ K}$, $2.3 \times 10^{-5} < \tau_{545} < 2.5 \times 10^{-5}$). This region of parameter space was arbitrarily chosen in order to obtain a large number of pixels within a narrow T_2 interval and small fractional range in τ_{545} . Black points represent the average observed intensities after rescaling each pixel to $\tau_{545} = 2.4 \times 10^{-5}$, while red error bars represent the typical per-pixel uncertainties at each frequency. For each pixel, the best-fit two-component model is derived via the MCMC procedure of Section 7.3, based on *Planck* 217–857 GHz and SFD 100 μm at full 6.1 resolution. Note that the two lowest-frequency data points were not used to derive the average two-component fit shown (blue line), while the three lowest-frequency data points were not used to derive the average Planck Collaboration et al. (2013a) single-MBB fit shown (cyan line). Bottom: comparison of average data, average two-component model and average Planck Collaboration et al. (2013a) single-MBB model after dividing out the average two-component model. Black error bars represent the uncertainty on the mean observed spectrum. The two-component fit is consistent with the average data from 100–3000 GHz, whereas extrapolating the Planck Collaboration et al. (2013a) model to 100–217 GHz yields predictions which are significantly low relative to the observed SED.

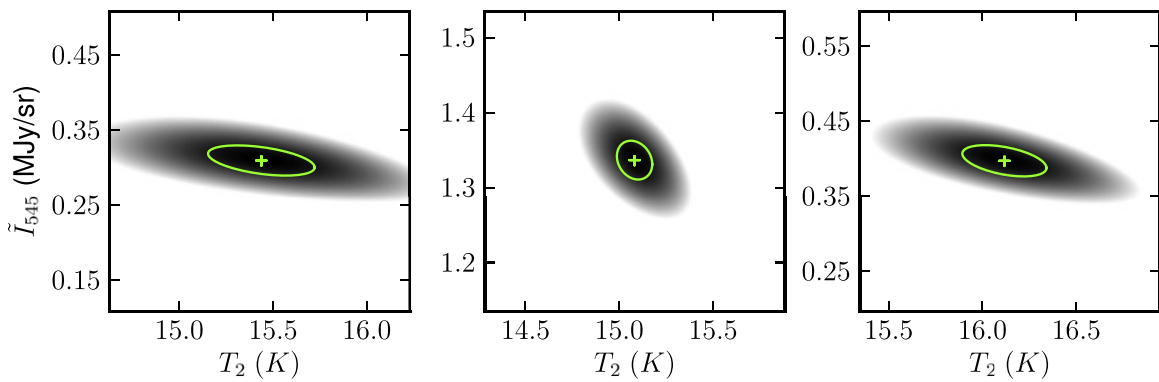


Figure 6. Gridded posterior PDFs for three $N_{\text{side}} = 2048$ HEALPix pixels, based on *Planck* 217–857 GHz and SFD 100 μm at full 6.1 resolution. The color scale is linear in $\log(P)$, with black corresponding to the maximum of $\log(P)$ and white representing $\max[\log(P)] - 5$. Light green crosses and ellipses mark the best-fit parameters and 1σ uncertainties based on our MCMC sampling of the posteriors. Our MCMC parameter and uncertainty estimates are in good agreement with those based on gridded posteriors. These three pixels are also representative in that we find the posterior distributions from Equation (11) are, in general, extremely well behaved, showing no multimodality or other pathological qualities. Left: low S/N pixel at high latitude in the Galactic north. Center: high S/N pixel in the Polaris flare region. Right: low S/N pixel at high latitude in the Galactic south.

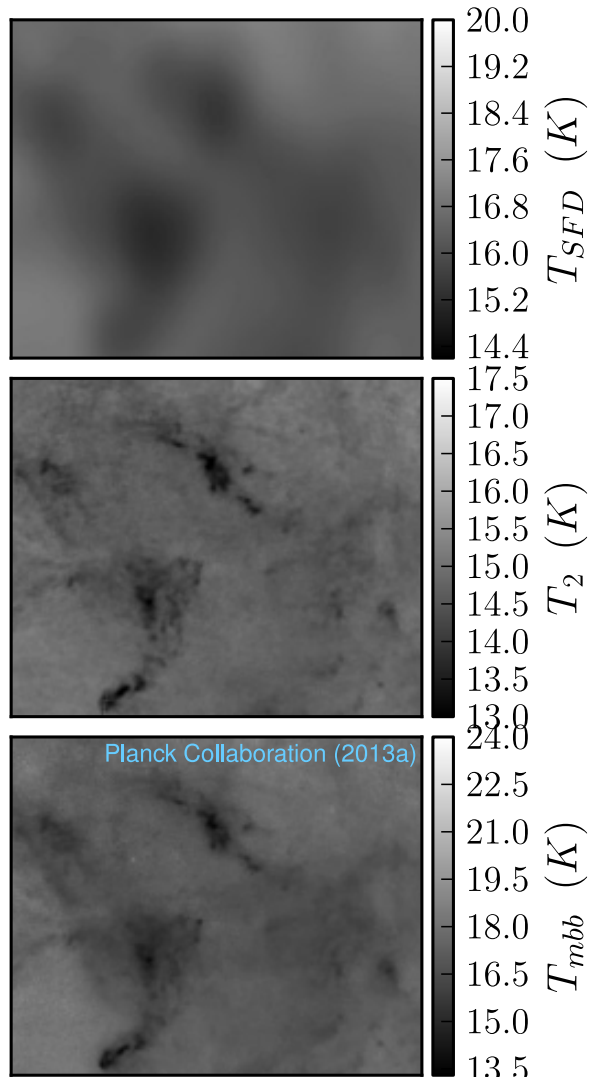


Figure 7. Comparison of temperature maps based on FIR dust emission over a 10.5×8.3 region centered about $(l, b) = (111^{\circ}6, 18^{\circ}3)$. Top: SFD temperature map based on DIRBE 100 μm and 240 μm , with ~ 1.3 resolution. Center: 6.1 resolution two-component temperature based on *Planck* 217–857 GHz and SFD 100 μm . Bottom: Planck Collaboration et al. (2013a) single-MBB temperature map based on *Planck* 353–857 GHz and 100 μm data, with 5.1 FWHM. Both temperature maps incorporating *Planck* observations clearly show a major improvement in angular resolution relative to SFD.

accuracy of the recovered parameters/uncertainties, and that the parameters/uncertainties ultimately derived are highly reliable. We can quantify the fidelity of our MCMC parameter estimates by noting that the rms fractional discrepancy between MCMC and gridded posterior means is 0.25% for \tilde{I}_{545} and 0.07% (~ 0.01 K) for T_2 . Regarding the accuracy of our uncertainty estimates, we find rms fractional discrepancies of 2.2% for $\sigma_{\tilde{I}_{545}}$ and 2.4% for σ_{T_2} . Aside from these small statistical scatters, we find no biases in our MCMC estimates of the parameters and their uncertainties.

7.4. Low-resolution Fits

As mentioned in Section 4, the combination of high S/N and high angular resolution afforded by the *Planck* HFI maps provides us with the opportunity to allow additional parameters of the two-component model, previously fixed by [FDS99](#), to vary spatially. Specifically, we consider allowing f_1 to vary, while maintaining β_1 , β_2 , and q_1/q_2 spatially constant. In principle, we could alternatively introduce a third free parameter by permitting β_1 , β_2 , or q_1/q_2 to vary while holding f_1 fixed. However, a model in which f_1 varies continuously from one line of sight to another is the most natural three-parameter scenario, in that f_1 variation can be attributed to continuous changes in the dust species' mass fractions, whereas continuous variations in the other global parameters, which represent grain emission/absorption properties, seem less plausible.

In order for our variable f_1 fits to remain sufficiently constrained following the introduction of a third free parameter, we enhance per-pixel S/N by smoothing the input maps to 1° FWHM, and pixelize at $N_{\text{side}} = 64$. To best constrain the model parameters in each pixel, we also include *Planck* 100 GHz and 143 GHz, and DIRBE 140 μm and 240 μm , all at 1° resolution.

We now run Markov chains sampling in all three of f_1 , \tilde{I}_{545} , and T_2 , with the posterior given by

$$P(\tilde{I}_{545}, T_2, f_1 | \mathbf{I}) \propto \mathcal{L}(\mathbf{I} | \tilde{I}_{545}, T_2, f_1) P(T_2) P(f_1). \quad (17)$$

The likelihood here is conceptually the same as that of Equation (12), but now depends on f_1 , which can vary from proposal to proposal within each individual pixel. The other difference is that \mathbf{I} and $\tilde{\mathbf{I}}$ now include 100 GHz, 143 GHz, 140 μm , and 240 μm , in addition to the five bands used for the full-resolution fits.

The prior $P(T_2)$ from Equation (16) remains unchanged. We adopt the following prior on f_1 :

$$P(f_1) = \mathcal{N}(f_1 | \bar{f}_1, \sigma_{\bar{f}_1}), \quad (18)$$

with $\bar{f}_1 = 0.0485$ (from Table 2, model 2) and $\sigma_{\bar{f}_1} = 0.005$. This is a fairly stringent prior, but we must restrict the fit from wandering with too much freedom, as we are attempting to constrain three parameters using an SED with only nine intensity measurements, several of which are quite noisy. Again, we have adopted a uniform prior on \tilde{I}_{545} , and, as mentioned previously, we have omitted it from Equation (17) as a matter of notation.

The resulting full-sky map of f_1 is shown in Figure 8. A general trend of increasing f_1 toward lower absolute Galactic latitudes is apparent. The other most salient features are the relatively low values of f_1 in the Polaris flare and R Coronae Australis regions, and the relatively high f_1 clouds near the north Galactic pole.

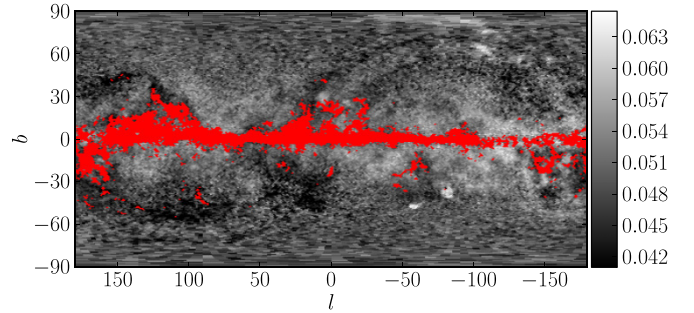


Figure 8. One degree FWHM full-sky map of f_1 derived from our low-resolution fits described in Section 7.4. Red coloring masks pixels with appreciable molecular emission, as defined in Section 3.4. Such pixels should not be trusted in this analysis, which is sensitive to the SED shape at low frequencies affected by CO line emission. Variations in f_1 along the ecliptic plane are spurious results of imperfect zodiacal light subtractions. However, interesting astrophysical variations of f_1 are evident, particularly the trend of increasing f_1 with decreasing absolute Galactic latitude, the relatively low f_1 values in the Polaris flare and R Coronae Australis regions, and the clouds with relatively high f_1 values near the north Galactic pole.

7.5. Global Parameters Revisited

The posterior sampling framework thus far described also affords us an opportunity to evaluate the goodness-of-fit for competing dust SED models, and thereby cross-check the conclusions of our correlation slope analysis in Section 6. The basic idea will be to continue evaluating the posterior of Equation (11), but at low resolution ($N_{\text{side}} = 64$), including all HFI bands as well as DIRBE 100 μm , 140 μm , and 240 μm , and switching to a uniform prior on T_2 . Under these circumstances, the chi-squared corresponding to the best-fit parameters for pixel p , termed χ_p^2 , is simply $-2 \times \log(P_{\max})$. We will refer to the per-pixel chi-squared per degree of freedom as $\chi_{p,v}^2$.

Because we seek to compare the goodness-of-fit for various dust SED models in the diffuse ISM, we restrict to a set of $\sim 10,800$ pixels ($\sim 22\%$ of the sky), with $|b| > 30^\circ$ and $|\beta| > 10^\circ$. We also avoid the SMICA inpainting mask, pixels with appreciable CO contamination, and compact sources. The goodness-of-fit “objective function” we employ to judge the quality of a particular dust SED model is $\langle \chi_{p,v}^2 \rangle$, where the average is taken over the aforementioned set of $\sim 10,800$ pixels. $\langle \chi_{p,v}^2 \rangle$ is also equivalent to the reduced chi-squared, χ_v^2 , when considering the total number of free parameters to be the number of pixels multiplied by the number of free parameters per pixel (and similarly for the total number of constraints), and taking $\chi^2 = \sum \chi_p^2$.

We calculate χ_v^2 for various dust SED models, independently minimizing each χ_p^2 by finding pixel p 's best-fitting dust temperature and normalization, then evaluating $\langle \chi_{p,v}^2 \rangle$. First, we consider single-MBB models with β spatially constant (see the black line in Figure 9). $\beta = 1.57$ yields the best fit, with $\chi_v^2 = 2.51$. This result is in excellent agreement with that of Section 6, where we found the best-fit single-MBB model to have $\beta = 1.59$.

We also evaluated χ_v^2 for single-MBB models in which β varies spatially. In these cases, we adopted the 0.5° resolution β map from Planck Collaboration et al. (2013a). We started by calculating χ_v^2 using the Planck Collaboration et al. (2013a) temperature map, finding $\chi_v^2 = 4.68$. Note that in this case no per-pixel chi-squared minimization was involved, as we simply evaluated χ_p^2 for each pixel based on the fully specified Planck Collaboration et al. (2013a) emission model. Next, we

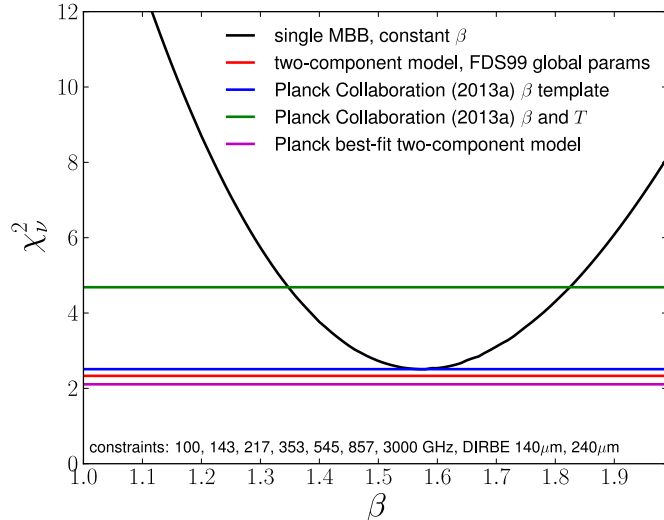


Figure 9. Comparison of goodness-of-fit, $\chi^2_{\nu} = \langle \chi^2_{\nu, \nu} \rangle$, for various dust SED models, as described in Section 7.5. For single-MBB models with spatially constant β , we varied β between 1 and 2 (horizontal axis), achieving reduced chi-squared χ^2_{ν} shown by the black line, with $\beta = 1.57$ providing the best single-MBB fit. Horizontal lines indicate χ^2_{ν} for other dust emission models considered, including the FDS99 best-fit two-component model (Table 2, model 1, red) and the Planck Collaboration et al. (2013a) single-MBB model (green). The minimum χ^2_{ν} is achieved with two-component “model 2” from Table 2 (magenta).

tested a single-MBB model for which we adopted the Planck Collaboration et al. (2013a) β map, but allowed the per-pixel temperature and normalization to vary so as to minimize χ^2_{ν} . In this case, we found $\chi^2_{\nu} = 2.51$, effectively identical to the value found for the spatially constant $\beta = 1.57$ single-MBB model. This is perhaps unsurprising, as the average β value from Planck Collaboration et al. (2013a) over the mask in question is $\langle \beta \rangle = 1.58$. This result does suggest, however, that in diffuse regions the half-degree variations in β are not materially improving the goodness-of-fit over the full frequency range 100–3000 GHz relative to a model with appropriately chosen spatially constant β .

We move on to evaluate two-component models, first calculating χ^2_{ν} with the FDS99 global parameters (Table 2, model 1). We find $\chi^2_{\nu} = 2.33$, a slight improvement relative to the best-fitting single-MBB models. Finally, we calculate χ^2_{ν} for Table 2, model 2, the two-component model favored by our *Planck*+DIRBE correlation slopes. In this case, we achieve the best goodness-of-fit out of all the models we have tested, with $\chi^2_{\nu} = 2.11$.

Thus, our degree-resolution goodness-of-fit analysis has generally confirmed the conclusions of Section 6. We find the single-MBB β value favored by the combination of *Planck* and DIRBE to be nearly identical here ($\beta = 1.57$) versus in Section 6 ($\beta = 1.59$). As in Section 6, we also find that the *Planck*+FIRAS and *Planck*+DIRBE best-fit two-component models from Table 2 outperform single-MBB alternatives, though only by a relatively small margin in χ^2_{ν} . Still, because our present analysis has $\sim 75,500$ dof, $\Delta\chi^2_{\nu} = 0.4$ formally corresponds to an enormously significant improvement in χ^2 . The agreement between our correlation slope analysis and the present goodness-of-fit analysis is especially encouraging for three main reasons: (1) in the present analysis, dust temperature has been allowed to vary on degree scales, whereas in Section 6 we assumed a single global dust temperature (2) the present analysis employs a fully detailed, per-pixel uncertainty model, and (3) in the present

analysis, our zero-level offsets factor into the dust temperature, whereas in Section 6 this was not the case, meaning the former and latter analyses agree in spite of their potential to be affected by rather different systematics.

8. OPTICAL REDDENING

While the temperature and optical depth maps thus far derived are useful for making thermal dust emission foreground predictions, estimating optical reddening/extinction is another important application of the τ_{545} map. Translating our two-component optical depth to reddening is especially valuable because our T_2 map has $\sim 13 \times$ better angular resolution than the SFD temperature correction, and thus there is reason to believe our two-component reddening estimates may be superior to those of SFD. However, as discussed in Section 11.2, we do not yet advocate for the wholesale replacement of SFD, and more detailed work is still necessary to determine/quantify the extent to which *Planck*-based dust maps might improve reddening estimates relative to SFD.

8.1. Reddening Calibration Procedure

We calibrate optical depth to reddening empirically rather than derive a relationship between τ_{545} and reddening by introducing additional assumptions about the dust grain physics and size distribution. To achieve this empirical calibration, we must adopt a set of calibrator objects for which true optical reddening is known. There are various possibilities at our disposal. Planck Collaboration et al. (2013a) calibrated their radiance and τ_{353} maps to $E(B - V)$ using broadband Sloan Digital Sky Survey (York et al. 2000) photometry for a set of $\sim 10^5$ quasars. The SFD calibration was originally tied to a sample of 384 elliptical galaxies, but was later revised by Schlafly & Finkbeiner (2011, hereafter SF11) based on $\sim 260,000$ stars with both spectroscopy and broadband photometry available from the SEGUE Stellar Parameter Pipeline (SSPP; Lee et al. 2008).

To calibrate our two-component optical depth to reddening, we make use of the stellar sample from SF11. Given a library of model stellar atmospheres, the spectral lines of these stars can be used to predict their intrinsic optical broadband colors. The “true” reddening is then simply the difference between the observed $g - r$ color and the $g - r$ color predicted from the spectral lines. Applying a color transformation then yields “true” $E(B - V)$ values for $\sim 260,000$ lines of sight. Throughout our SSPP calibration analysis, we restrict to the $\sim 230,000$ lines of sight with $|b| > 20^\circ$ in order to avoid stars that may not lie behind the full dust column. In this section and Section 8.2, we make absolute latitude cuts (in both b and β) at 20° , to match the footprint of SF11 and adapt to the non-uniform distribution of SSPP stars on the sky. The calibration of two-component optical depth to $E(B - V)$ is performed as a linear regression of $E(B - V)_{\text{SSPP}}$ versus τ_{545} . τ_{545} is considered to be the independent variable in this regression, as we ultimately wish to predict $E(B - V)$ as a function of optical depth, and τ_{545} has much higher S/N than the SSPP $E(B - V)$ estimates.

This regression is illustrated in Figure 10. As expected, there is a strong linear correlation between $E(B - V)_{\text{SSPP}}$ and τ_{545} . The conversion factor from τ_{545} to $E(B - V)$ is 2.62×10^3 . Reassuringly, the best-fit offset is close to zero, ~ 2.6 mmag.

Figure 11 shows the residuals of our τ_{545} -based reddening predictions, $E(B - V)_{\text{2comp}}$, relative to the corresponding SF11 reddening measurements, $E(B - V)_{\text{SSPP}}$, as a function of SFD reddening, $E(B - V)_{\text{SFD}}$, (top left panel) and as a function

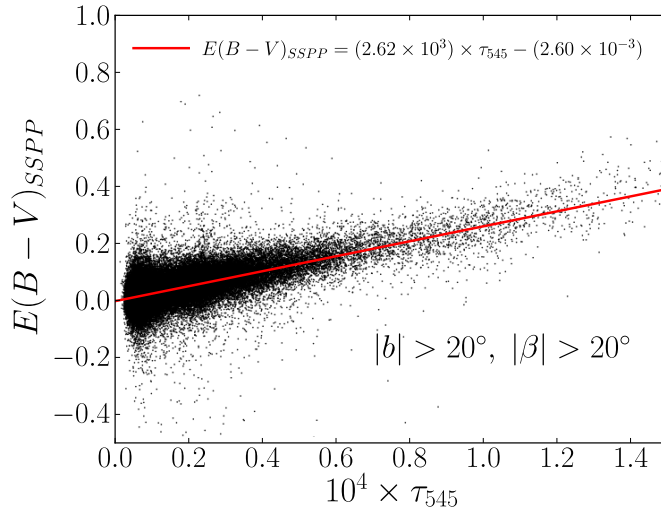


Figure 10. Linear fit of $E(B - V)_{\text{SSPP}}$ as a function of two-component 545 GHz optical depth, illustrating our procedure for calibrating optical depth to reddening, as described in Section 8.1.

of hot dust temperature (bottom left panel). For comparison, the right panels show analogous residual plots, but with respect to reddening predictions based on our calibration of the Planck Collaboration et al. (2013a) 353 GHz optical depth to $E(B - V)_{\text{SSPP}}$, using the same regression procedure employed

to calibrate $E(B - V)_{\text{2comp}}$. We refer to these reddening predictions based on the Planck Collaboration et al. (2013a) single-MBB model and calibrated to the SF11 measurements as $E(B - V)_{\text{mbb}}$.

All four residual plots in Figure 12 show systematic problems at some level. The most striking systematic trend is the “bending” behavior of the reddening residuals versus $E(B - V)_{\text{SFD}}$ (top panels), with the median residual bottoming out near -10 mmag at $E(B - V)_{\text{SFD}} \approx 0.15$ mag. This behavior is common to both $E(B - V)_{\text{2comp}}$ and $E(B - V)_{\text{mbb}}$, and in fact was first noted in the residuals of $E(B - V)_{\text{SFD}}$ itself relative to $E(B - V)_{\text{SSPP}}$ by SF11 (see their Figure 6). Such a bending behavior is troubling because it could indicate a nonlinearity common to many FIR reddening predictions based on column densities inferred from dust emission. Alternatively, because the SF11 stars are distributed over the sky in a highly non-uniform manner, the bend could arise from aliasing of discrepancies particular to certain sky regions (e.g., inner versus outer Galaxy) on to the $E(B - V)_{\text{SFD}}$ axis.

The obvious culprit for any potential nonlinearity in FIR-based reddening estimates is a faulty temperature correction. For this reason, we have included the bottom panels of Figure 11, to check for the presence of a temperature dependence of the reddening residuals. Indeed, in both the two-component and single-MBB cases there exists some systematic dependence of the reddening residuals on temperature. For $T_{\text{mbb}} \gtrsim 19$ K, the median residual is reasonably flat, but at lower temperatures (the lowest temperature $\sim 20\%$ of SSPP sight lines), the median

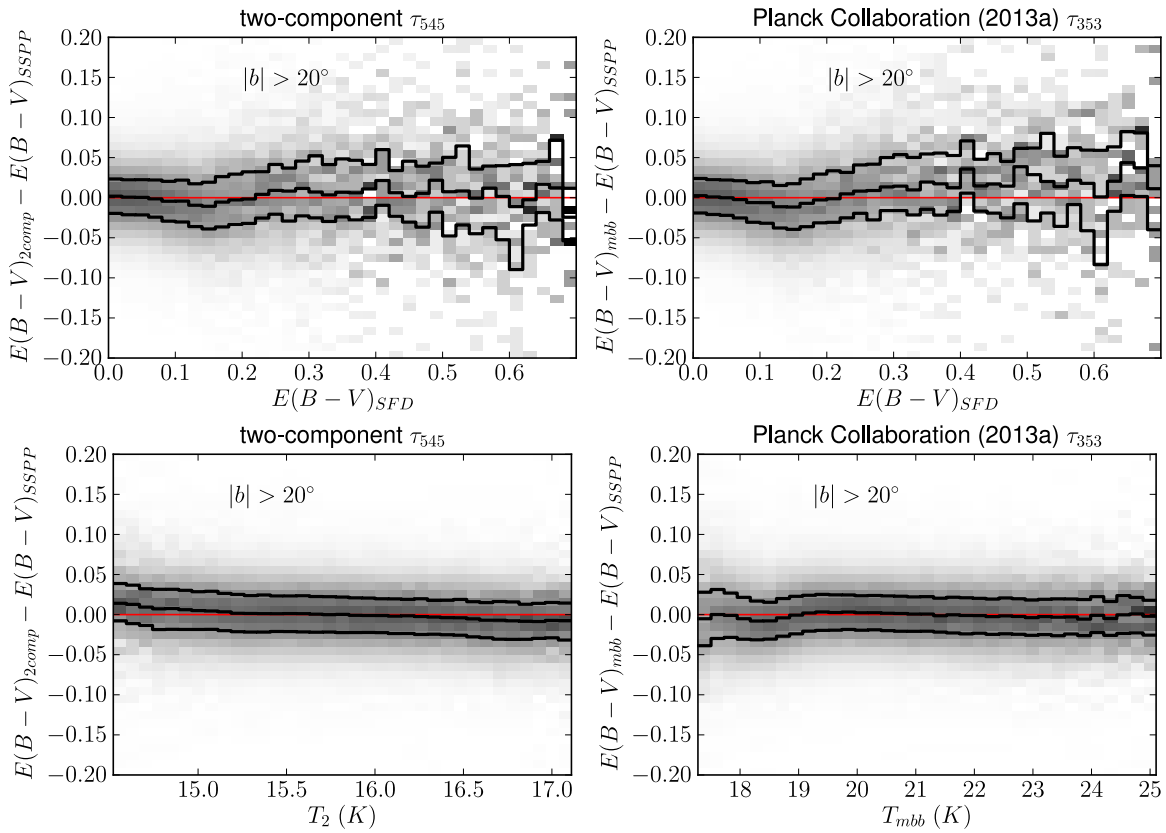


Figure 11. Top left: residuals of $E(B - V)_{\text{2comp}}$ relative to $E(B - V)_{\text{SSPP}}$ as a function of $E(B - V)_{\text{SFD}}$. The grayscale represents the conditional probability within each $E(B - V)_{\text{SFD}}$ bin. The central black line shows the moving median. The upper and lower black lines represent the moving 75th and 25th percentiles, respectively. Bottom left: residuals of $E(B - V)_{\text{2comp}}$ relative to $E(B - V)_{\text{SSPP}}$ as a function of hot dust temperature T_2 . Top right: same as the top left, but illustrating the residuals of $E(B - V)_{\text{mbb}}$, our calibration of the Planck Collaboration et al. (2013a) τ_{353} to $E(B - V)_{\text{SSPP}}$. Bottom right: same as the bottom left, but showing the $E(B - V)_{\text{mbb}}$ residuals as a function of the single-MBB dust temperature from Planck Collaboration et al. (2013a). The temperature axes always range from the 0.4th percentile temperature value to the 99.6th percentile temperature value.

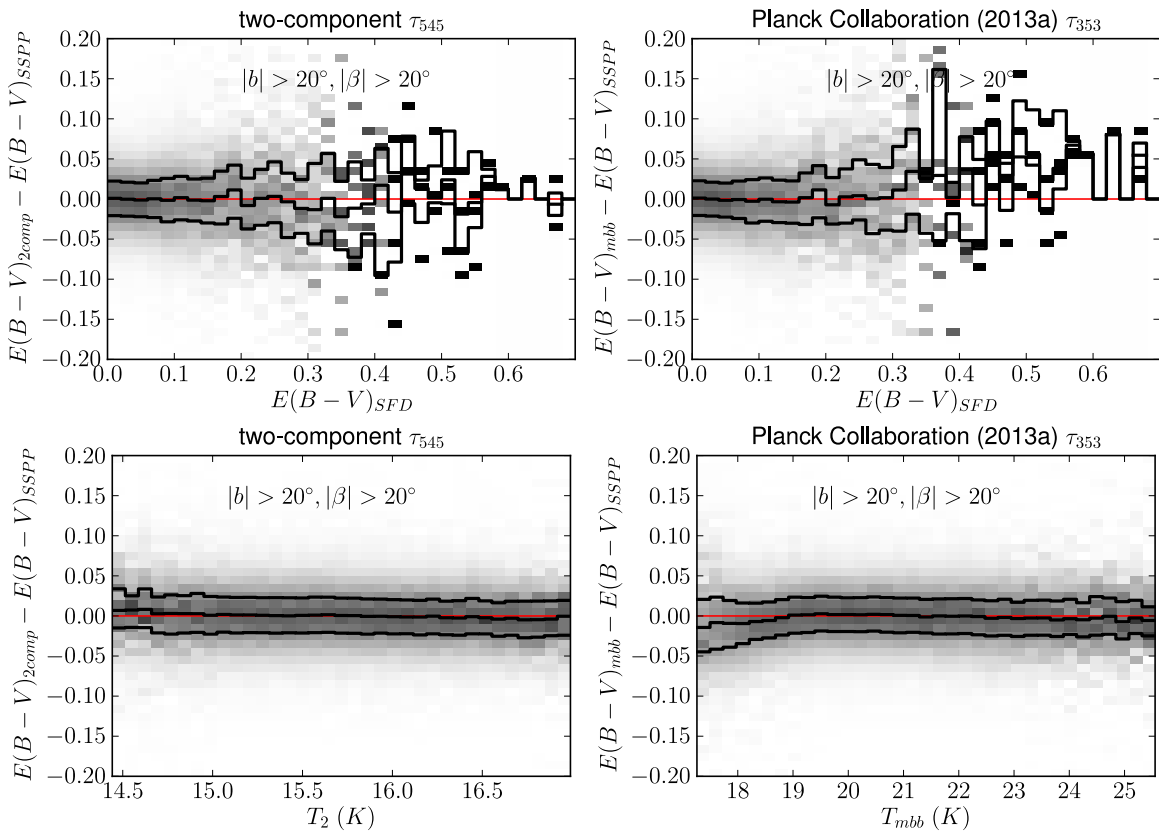


Figure 12. Same as Figure 11, but restricting to high ecliptic latitude, $|\beta| > 20^\circ$. In both the top left and top right plots, the bending of the reddening residuals as a function of $E(B - V)_{SFD}$ seen in Figure 11 has been eliminated. Further, the two-component reddening residual temperature dependence (bottom left) has been significantly reduced relative to the corresponding trend shown in Figure 11. For $E(B - V)_{SFD} \gtrsim 0.3$ mag, the top row plots appear noisy because there are an insufficient number of remaining SSPP points of comparison.

shows trends at the ~ 10 mmag level. On the other hand, the median residual in the two-component case trends downward with increasing T_2 over the entire T_2 range shown, with a peak-to-peak amplitude of ~ 20 mmag.

8.2. Rectifying the Reddening Residuals

In this section we describe our attempts to eliminate the systematic problems in the two-component reddening residuals shown in the left column of Figure 11. We employed two main strategies: (1) recomputing the two-component τ_{545} by re-running our Markov chains after modifying the input maps and/or changing the particular two-component model parameters adopted and (2) making spatial cuts to isolate sky regions in which the residuals are especially pristine (or especially problematic).

The following is a list of dust model modifications we tested that proved to have little impact on the reddening residual trends as a function of either $E(B - V)_{SFD}$ or T_2 :

1. Varying each of the global two-component model parameters β_1 , β_2 , q_1/q_2 , and f_1 individually while holding the others fixed.
2. Allowing f_1 to vary spatially as in the fits of Section 7.4.
3. Changing the mean and/or variance of the T_2 prior.
4. Varying multiple global parameters at a time, e.g., both f_1 and q_1/q_2 , restricting to regions of parameter space favored by our goodness-of-fit analyses described in Sections 6 and 7.5.

We additionally investigated the following spatial cuts, which did not resolve the dominant problems noted in the reddening residuals:

1. Separating celestial north and south.
2. Separating Galactic north and south.
3. Separating inner and outer Galaxy.
4. Combining the above two sets of cuts, i.e., separating the Galaxy into quadrants.
5. Combining these spatial cuts with the dust model changes of the previous list.

However, we found that changing the zero-level offsets of the input maps had a significant effect on the strength of the anticorrelation between median reddening residual and T_2 . In particular, we experimented with perturbing the zero-level offset of *Planck* 857 GHz while correspondingly changing the zero levels of the remaining *Planck* maps based on the prescription of Section 3.5.2. We also experimented with changing the zero level of SFD i100, independent of the other zero levels. Unfortunately, completely flattening the reddening residual dependence on T_2 required unreasonably large zero-level modifications. For example, flattening the T_2 residual required adding $\gtrsim 0.6$ MJy sr $^{-1}$ to the i100 map. Such an offset is implausible, being an order of magnitude larger than the nominal i100 zero-level uncertainty quoted by SFD, and comparable to the entire 3000 GHz CIB monopole signal. Furthermore, we note that even these large zero-level modifications had virtually no effect in eliminating the reddening residual “bend” versus $E(B - V)_{SFD}$. Thus, changing the zero-level offsets showed hints of promise in rectifying the reddening residual temperature dependence, but

could not by itself completely resolve the systematic trends in reddening residuals.

The only solution we have been able to identify that both removes the “bend” versus $E(B - V)_{\text{SFD}}$ and simultaneously reduces the temperature dependence of the reddening residuals is cutting out the ecliptic plane by restricting to $|\beta| > 20^\circ$. In this case, we completely eliminated the bending behavior of the residual versus $E(B - V)_{\text{SFD}}$, and significantly reduced the T_2 dependence to a peak-to-peak amplitude of only ~ 10 mmag (see Figure 12). Figure 12 still includes the single-MBB plots (right column), to show that the bend versus $E(B - V)_{\text{SFD}}$ is eliminated by the $|\beta|$ cut, even for the single-MBB model. However, the single-MBB residuals still differ systematically from zero for $T \lesssim 19$ K. Perhaps the improvements in the two-component reddening residuals after restricting to high ecliptic latitude should come as no surprise, given that the ecliptic plane is the most obvious systematic problem with our temperature map (see the full-sky results shown in Figure 16).

After cutting the ecliptic plane, we found that only small zero-level perturbations were required to fully flatten the temperature residuals, while still maintaining flat residuals versus $E(B - V)_{\text{SFD}}$. The optimal offsets we found were ± 0.08 MJy sr $^{-1}$ to 100 and 857 GHz, respectively (see Figure 13). These offsets are well within reason, given the nominal zero-level uncertainties quoted in Table 1.

9. COMPARISON OF EMISSION PREDICTIONS

9.1. The 353–3000 GHz Frequency Range

Here we compare our two-component emission predictions to those of the Planck Collaboration et al. (2013a) single-MBB model in the 353–3000 GHz range. This frequency range represents the overlap between the recommended range of applicability for the Planck Collaboration et al. (2013a) model and the 100–3000 GHz frequency range of our two-component model. Since we have used input maps that are very similar to those of Planck Collaboration et al. (2013a), and since our model and the Planck Collaboration et al. (2013a) model both fit the data well in this frequency range, good agreement between our two-component predictions and those of the Planck Collaboration et al. (2013a) single-MBB model is to be expected.

We compare the emission models in this frequency range by using each model in turn to predict the observed *Planck* 353, 545, and 857 GHz maps, as well as the 3000 GHz DIRBE/IRAS map. We rebin to $N_{\text{side}} = 64$ and restrict to the diffuse sky regions of our mask from Section 7.5. We summarize this comparison by producing a per-band scatter plot of the Planck Collaboration et al. (2013a) prediction versus the two-component prediction, and performing a linear regression between these two quantities, as shown in Figure 14. Before plotting and performing these regressions, we adjusted the Planck Collaboration et al. (2013a) predictions to account for the differing zero-level offsets used in this work and in Planck Collaboration et al. (2013a). For instance, at 3000 GHz, Planck Collaboration et al. (2013a) added 0.17 MJy sr $^{-1}$ to the SFD zero level, whereas we made no such modification; therefore, for the sake of comparison, we subtracted 0.17 MJy sr $^{-1}$ from the Planck Collaboration et al. (2013a) predictions before plotting and performing the 3000 GHz regression.

The slopes obtained from these linear fits indicate very good agreement between the single-MBB and two-component models, with values between 0.983–1.015 (agreement at the

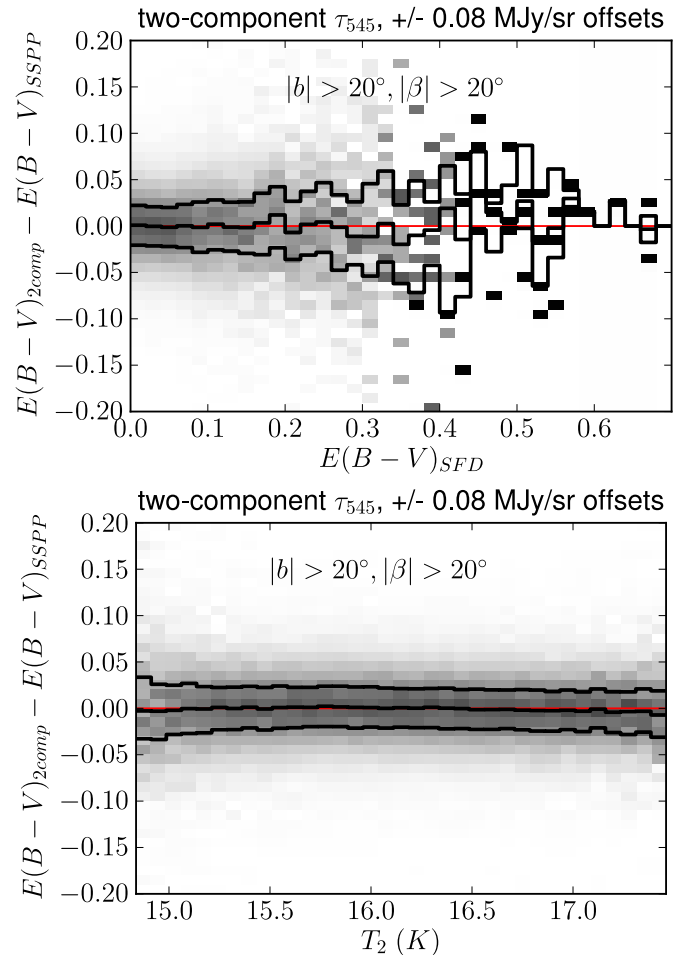


Figure 13. Two-component reddening residuals after restricting to high ecliptic latitude ($|\beta| > 20^\circ$) and perturbing the 100 and 857 GHz zero levels by $+0.08$ MJy sr $^{-1}$ and -0.08 MJy sr $^{-1}$, respectively. The bending behavior as a function of $E(B - V)_{\text{SFD}}$ has been eliminated, and virtually no temperature dependence remains. For $E(B - V)_{\text{SFD}} \gtrsim 0.3$ mag, the top plot appears noisy because there are an insufficient number of remaining SSPP points of comparison following our cut on ecliptic latitude.

$\leq 1.7\%$ level). The offsets are also consistent with zero to within the uncertainties quoted in Table 1. We do not find evidence that our two-component model provides emission predictions in the 353–3000 GHz range which are superior to those of Planck Collaboration et al. (2013a). From 353–3000 GHz and in diffuse sky regions, the main difference between emission predictions from these two models will be overall offsets due to differing input map zero levels.

9.2. The 100–217 GHz Frequency Range

FDS99 originally performed their FIRAS+DIRBE dust SED analysis for the sake of accurately forecasting low-frequency CMB foregrounds. Recently, Galactic CMB foregrounds, especially in the 100–150 GHz frequency range, have become a focal point of cosmology owing to the Ade et al. (2014) B -mode polarization results. Here we show that our two-component foreground predictions remain accurate on average to within 2.2% from 100 to 217 GHz, and we quantify the benefit of using our two-component emission predictions in this frequency range relative to extrapolating the Planck Collaboration et al. (2013a) single-MBB model.

To assess the accuracy of low-frequency emission predictions, we compare the observed *Planck* HFI map at each of 100,

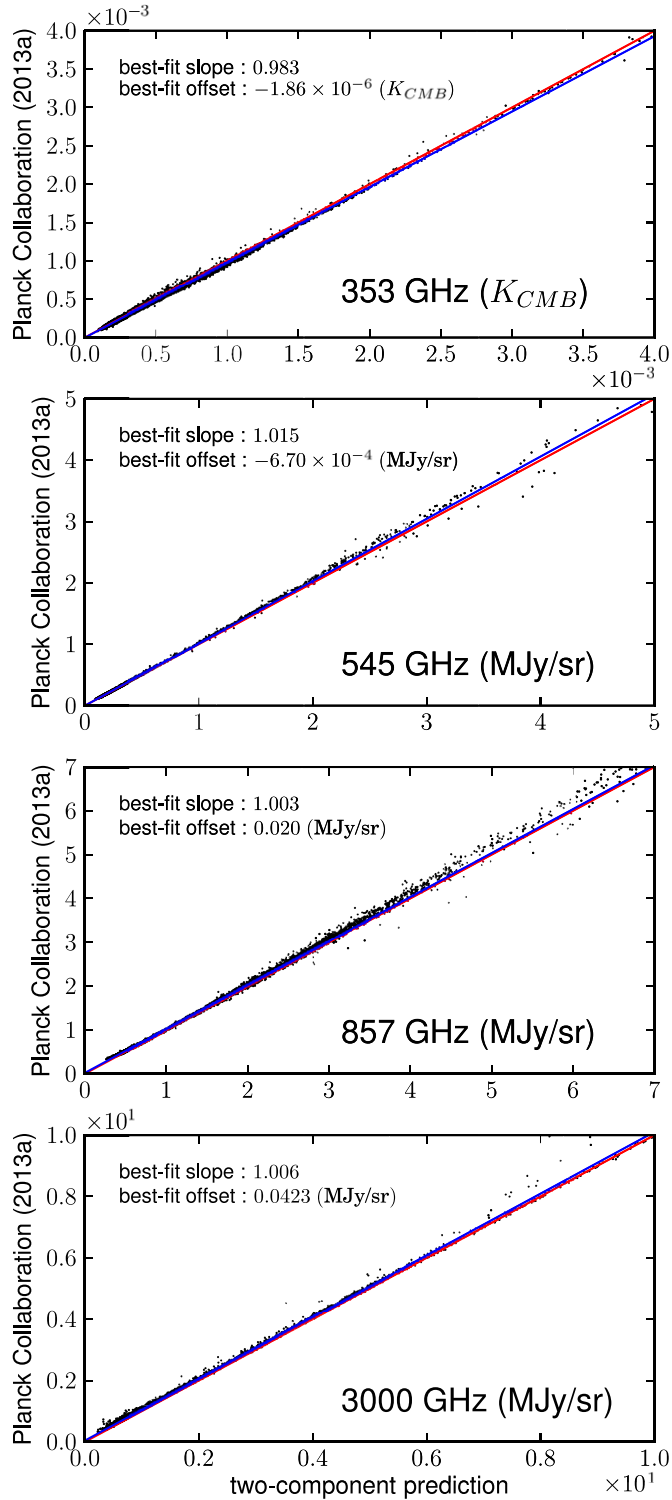


Figure 14. Scatter plots of Planck Collaboration et al. (2013a) single-MBB predictions (vertical axes) vs. our two-component predictions (horizontal axes), rebinning to $N_{\text{side}} = 64$ and restricting to the diffuse regions of Section 7.5. The lines of best fit are shown in blue, and red lines represent perfect agreement between the two predictions. Note that a per-band offset has been applied to the Planck Collaboration et al. (2013a) predictions to account for the differing zero-level offsets used in building the two models. After accounting for the different zero levels, the best-fit offsets between predictions are consistent with zero to within the uncertainties quoted in Table 1. The slopes are also very nearly unity, to within $\leq 1.7\%$.

143, 217 GHz to the corresponding single-MBB and two-component predictions, with all maps smoothed to 1° FWHM and binned down to $N_{\text{side}} = 64$. We restrict to the same set of pixels used for the goodness-of-fit analysis of Section 7.5, with $|b| > 30^\circ$ and $|\beta| > 10^\circ$, also avoiding molecular emission, the SMICA inpainting mask, and compact sources. We then perform a linear fit between the *Planck* observed emission and the predicted emission at each frequency and for each emission model. For these fits, we consider the predicted emission to be the independent variable, since it has higher S/N than the observations, especially at 100 and 143 GHz. We also assign pixel weights proportional to the predicted emission, so that the best-fit lines faithfully capture the linear trend exhibited without being biased by the large number of very low S/N pixels with minimal emission. Scatter plots between the predicted and observed emission are shown in Figure 15. The best-fit lines are overplotted and their equations are given in the top left corner of each subplot.

In both the single-MBB and two-component cases, all of the best-fit offsets are within the uncertainties quoted in Table 1. On the other hand, the top row of Figure 15 shows that the Planck Collaboration et al. (2013a) single-MBB extrapolations yield slopes substantially different from unity: 1.079 at 217 GHz, 1.126 at 143 GHz, and 1.188 at 100 GHz. The fact that the slopes are larger than unity indicates that the Planck Collaboration et al. (2013a) extrapolations are systematically low. The systematic underprediction evidently becomes gradually more pronounced as lower frequencies are considered, with a 7.9% underprediction at 217 GHz, a 12.6% underprediction at 143 GHz, and an 18.8% underprediction at 100 GHz. A deficit in single-MBB predictions relative to the observed *Planck* 100–217 GHz emission was also noted in Planck Collaboration et al. (2011a), e.g., their Figure 7.

For the case of the two-component model, we perform full-resolution 217–3000 GHz fits using the *Planck*+DIRBE favored global parameters (Table 2, model 2), then smooth to 1° FWHM and bin down to $N_{\text{side}} = 64$ before predicting the 100–217 GHz emission. The bottom row of Figure 15 shows that each of the best-fit lines is very similar to the corresponding red line which represents a perfect match between predicted and observed emission. More quantitatively, the two-component slopes are all within 2.2% of unity: 0.978 at 217 GHz, 0.986 at 143 GHz, and 1.022 at 100 GHz. We note that at 217 GHz, the good agreement is in some sense predetermined by the fact that *Planck* 217 GHz has been included in our two-component MCMC fits. On the other hand, the 143 and 100 GHz predictions are based on extrapolation.

We conclude from these predicted versus observed emission comparisons that our two-component model outperforms extrapolation of the Planck Collaboration et al. (2013a) single-MBB model at predicting Galactic thermal dust emission in diffuse regions from 100–217 GHz. It should be reiterated, once again, that Planck Collaboration et al. (2013a) did not intend for their single-MBB model to be extrapolated to frequencies below 350 GHz (see their Section 7.2.1), whereas we optimized our two-component model to be valid over the entire 100–3000 GHz frequency range. Our two-component model thus represents the first *Planck* based thermal dust emission model valid over the entire 100–3000 GHz frequency range.

10. DATA RELEASE

We are releasing a set of $N_{\text{side}} = 2048$ HEALPix maps in Galactic coordinates that summarize the results of our

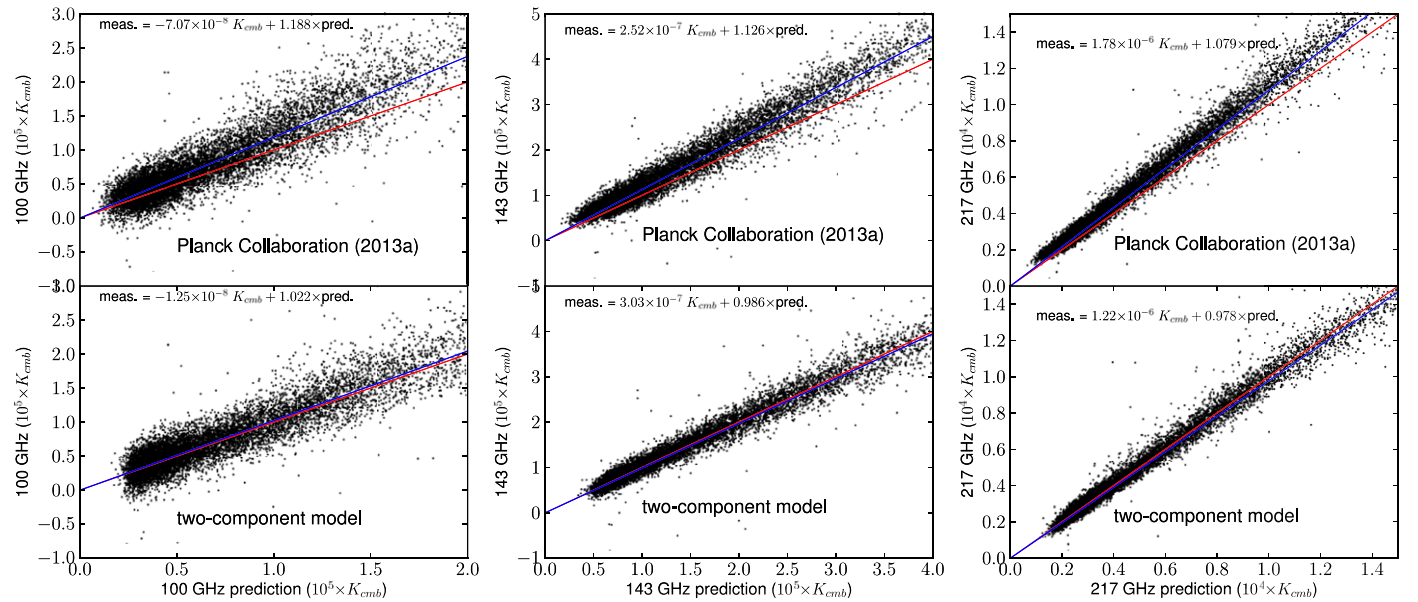


Figure 15. Comparison between low-frequency thermal dust emission predictions from our best-fit two-component model (Table 2, model 2) and those based on extrapolation of the Planck Collaboration et al. (2013a) model. The top row shows scatter plots of the Planck Collaboration et al. (2013a) predictions vs. observed *Planck* 100 GHz (left), *Planck* 143 GHz (center), and *Planck* 217 GHz (right). The bottom row shows scatter plots of the corresponding two-component predictions vs. *Planck* observations. In all cases, the blue line indicates the best-fit linear relationship, while the red line represents a perfect match between predictions and observations. The lines of best fit illustrate that the single-MBB model systematically underpredicts emission (in the multiplicative sense) by 18.8%, 12.6%, and 7.9% at 100, 143, and 217 GHz, respectively. On the other hand, by the same metric, the two-component model predictions at 100–217 GHz are always accurate to within $\leq 2.2\%$. The two-component fit results shown are based on 217–3000 GHz observations, meaning that the 100 GHz and 143 GHz predictions are truly extrapolations, while the 217 GHz agreement is enforced by the fitting process itself to some extent.

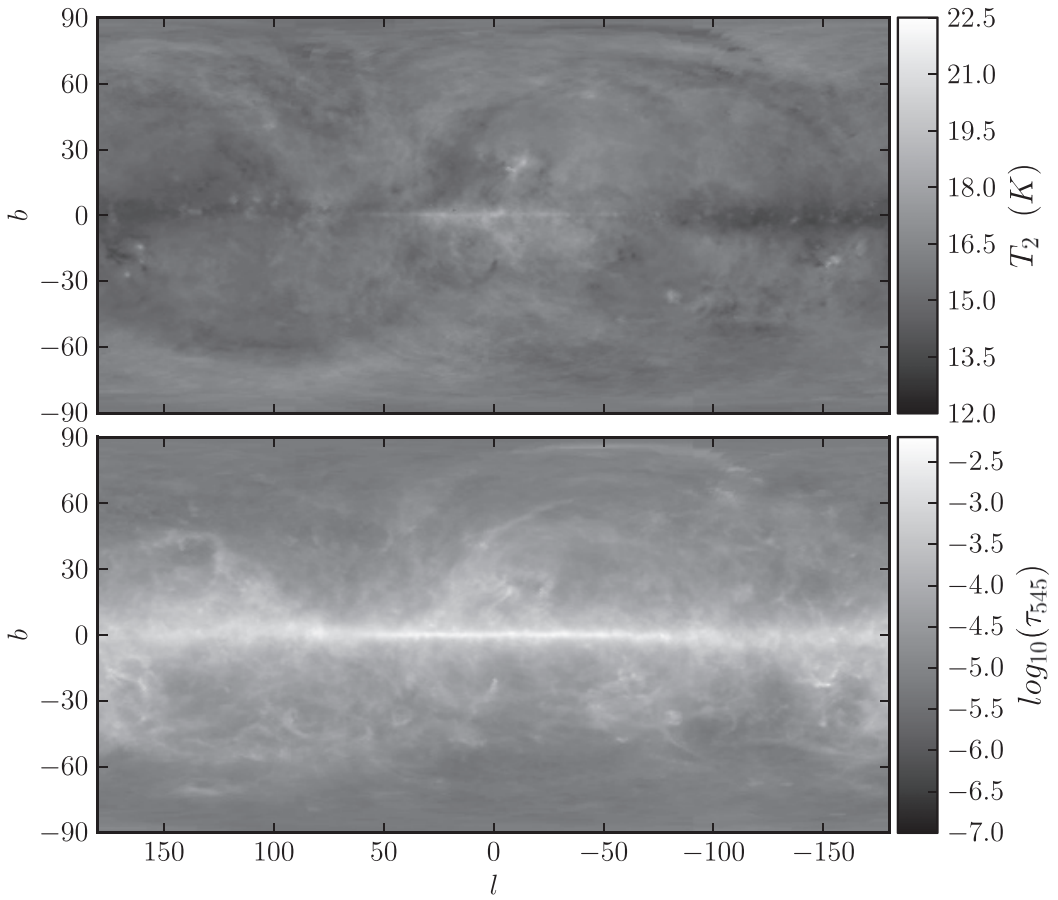


Figure 16. Top: hot dust temperature derived from our full-resolution two-component model fits of *Planck* 217–857 GHz and SFD 100 μ m, downbinned to 27' resolution. Bottom: corresponding full-sky map of best-fit two-component 545 GHz optical depth.

full-resolution two-component dust fits. Low-resolution renderings of our full-sky dust temperature and optical depth maps are shown in Figure 16. Our data release also includes software utilities for obtaining emission and reddening predictions from our *Planck*-based two-component fits. Refer to the data release documentation and FITS file headers for further details.³

11. CONCLUSIONS

11.1. Single-MBB versus Two-component Emission

A major aim of this work has been to determine whether the **FDS99** two-component dust emission model remains favored over single-MBB models when swapping the *Planck* HFI maps for FIRAS at frequencies below 1250 GHz. We compared dust SED models in two ways: (1) by fitting a 100–3000 GHz spectrum composed of per-band correlation slopes versus *Planck* 857 GHz, (2) by finding the best-fit dust temperature and optical depth per line-of-sight, with each pixel’s SED comprised of 100–3000 GHz *Planck*+DIRBE data, and comparing the average goodness-of-fit under various emission models.

In both the correlation slope analysis of Section 6 and the goodness-of-fit analysis of Section 7.5 we found that the best-fit *Planck*+DIRBE two-component model (Table 2, model 2) outperformed the best-fit single-MBB model, but by a lesser margin in χ^2_v than found by **FDS99** using FIRAS+DIRBE. Specifically, our best-fit *Planck*+DIRBE two-component model yielded an improvement of $\Delta\chi^2_v = 3.41$ (Section 6) and $\Delta\chi^2_v = 0.4$ (Section 7.5). This represents a far less dramatic contrast in χ^2_v than found by the **FDS99** correlation slope analysis, $\Delta\chi^2_v = 29.2$. Perhaps a relative lack of discrimination among competing dust SED models when relying on *Planck*+DIRBE is to be expected, given that our constraints include only nine broad frequency channels, whereas **FDS99** employed >200 narrow bands. Still, $\Delta\chi^2_v = 0.4$ from Section 7.5 is formally of enormous significance, given the $\sim 75,000$ dof in that analysis.

Nevertheless, we have established that the two-component emission model remains viable in light of the *Planck* HFI data, and that the FIR/submillimeter dust SED’s preference for two MBB components rather than just one is not simply an idiosyncrasy of the FIRAS spectra. Furthermore, we showed in Section 9.2 that our 100–217 GHz two-component emission predictions are on average accurate to within 2.2%, whereas extrapolating the Planck Collaboration et al. (2013a) single-MBB model systematically underestimates low-frequency dust emission by 18.8% at 100 GHz, 12.6% at 143 GHz, and 7.9% at 217 GHz. We therefore recommend that those interested in thermal dust foregrounds in the 100–3000 GHz frequency range use our data release to predict unpolarized dust emission, at the very least in order to help determine the level at which the choice of dust emission model may influence their conclusions.

11.2. Toward a Replacement for SFD

Because of the broad frequency coverage and high angular resolution afforded by the *Planck* HFI full-sky maps, we initially speculated that a *Planck* based extinction map might easily outperform SFD, the most commonly used optical reddening map. However, at this point in time, we do not yet recommend that the results presented in this work be considered a replacement for SFD in terms of optical extinction/reddening estimates.

The CIBA remains a major imperfection that still requires further investigation. The CIB anisotropies are very evident in

low-dust regions of our maps of optical depth and predicted dust emission. As described in Section 7.3, we have propagated the CIBA rms amplitudes and inter-frequency covariances into our uncertainty estimates through the likelihood function in our MCMC procedure. However, this treatment falls far short of actually removing the spatial imprint of the CIBA on our derived parameters. The CIB anisotropies are more prominent in our optical depth map relative to that of SFD because of the lower-frequency *Planck* maps we rely upon to achieve a high-resolution temperature correction.

Imperfect zodiacal light (zodi) corrections represent a second major limitation of our results. The ecliptic plane’s prominence in our full-sky temperature map (Figure 16) suggests that the zodiacal light subtractions performed on the input maps are not ideal. Our comparisons of the FIR maps used in this study against H α emission bear out this notion, further revealing that the imperfect zodi corrections are not limited to i100, but in fact are noticeable in all of the HFI R1.10_nominal_ZodiCorrected maps as well. We deemed it infeasible to reconsider all of the *Planck* zodi corrections in addition to the 3000 GHz zodi correction as a part of this study, especially considering that the forthcoming *Planck* 2014 release is expected to include a revised/improved zodi subtraction.

Irrespective of the notable imperfections in our results, more detailed comparisons between our reddening estimates here and those of SFD are required to determine/quantify which map is superior in particular applications. One definitive improvement of our reddening estimates relative to those of SFD is our ability to quote reddening uncertainties, which results from the probabilistic framework of Section 7.3. The extinction estimates from this work can also be employed as an alternative to those of SFD, to gauge the impact of dust map choice in a specific end user’s application.

We thank the anonymous referee for helpful suggestions. We gratefully acknowledge support from the National Science Foundation Graduate Research Fellowship under grant No. DGE1144152, and NASA grant NNX12AE08G. Based on observations obtained with *Planck*, (<http://www.esa.int/Planck>), an ESA science mission with instruments and contributions directly funded by ESA Member States, NASA, and Canada. This research made use of the NASA Astrophysics Data System (ADS) and the IDL Astronomy User’s Library at Goddard (available at <http://idlastro.gsfc.nasa.gov>).

REFERENCES

- Ade, P., Aikin, R. W., Barkats, D., et al. 2014, *PhRvL*, **112**, 241101
- Boggess, N. W., Mather, J. C., Weiss, R., et al. 1992, *ApJ*, **397**, 420
- Doi, Y., Komugi, S., Kawada, M., et al. 2012, *PKAS*, **27**, 111
- Draine, B. T., & Li, A. 2007, *ApJ*, **657**, 810
- Finkbeiner, D. P., Davis, M., & Schlegel, D. J. 1999, *ApJ*, **524**, 867
- Górski, K. M., Hivon, E., Banday, A. J., et al. 2005, *ApJ*, **622**, 759
- Hauser, M. G., & Dwek, E. 2001, *ARA&A*, **39**, 249
- Kalberla, P. M. W., Burton, W. B., Hartmann, D., et al. 2005, *A&A*, **440**, 775
- Lee, Y. S., Beers, T. C., Sivarani, T., et al. 2008, *AJ*, **136**, 2022
- Low, F. J., Young, E., Beintema, D. A., et al. 1984, *ApJL*, **278**, L19
- Mather, J. C. 1982, *OptEn*, **21**, 769
- Meisner, A. M., & Finkbeiner, D. P. 2014, *ApJ*, **781**, 5
- Planck Collaboration, Abergel, A., Ade, P. A. R., et al. 2013a, *A&A*, **571**, A11
- Planck Collaboration, Ade, P. A. R., Aghanim, N., et al. 2011a, *A&A*, **536**, A19
- Planck Collaboration, Ade, P. A. R., Aghanim, N., et al. 2011b, *A&A*, **536**, A18
- Planck Collaboration, Ade, P. A. R., Aghanim, N., et al. 2013b, *A&A*, **571**, A1
- Planck Collaboration, Ade, P. A. R., Aghanim, N., et al. 2013c, *A&A*, **571**, A9
- Planck Collaboration, Ade, P. A. R., Aghanim, N., et al. 2013d, *A&A*, **571**, A7
- Planck Collaboration, Ade, P. A. R., Aghanim, N., et al. 2013e, *A&A*, **571**, A8

³ <http://planck.skymaps.info>

- Planck Collaboration, Ade, P. A. R., Aghanim, N., et al. 2013f, [A&A](#), **571**, A12
Planck Collaboration, Ade, P. A. R., Aghanim, N., et al. 2013g, [A&A](#), **571**, A13
Planck Collaboration, Ade, P. A. R., Aghanim, N., et al. 2013h, [A&A](#), **571**, A14
Planck Collaboration, Ade, P. A. R., Aghanim, N., et al. 2013i, [A&A](#), **571**, A30
Planck Collaboration, Ade, P. A. R., Aghanim, N., et al. 2014, arXiv:[1409.2495](#)
Reach, W. T., Dwek, E., Fixsen, D. J., et al. 1995, [ApJ](#), **451**, 188
Schlafly, E. F., & Finkbeiner, D. P. 2011, [ApJ](#), **737**, 103
Schlafly, E. F., Green, G., Finkbeiner, D., et al. 2014, [ApJ](#), **789**, 15
Schlegel, D. J., Finkbeiner, D. P., & Davis, M. 1998, [ApJ](#), **500**, 525
Wheelock, S. L., Gautier, T. N., Chillemi, J., et al. 1994, STIN, **95**, 22539
Wright, E. L., Eisenhardt, P. R. M., Mainzer, A. K., et al. 2010, [AJ](#), **140**, 1868
York, D. G., Adelman, J., Anderson, J. E., Jr., et al. 2000, [AJ](#), **120**, 1579